Nonlinear Dyn
https://doi.org/10.1007/s11071-022-07721-y

ORIGINAL PAPER

Internal resonance in a MEMS levitation force resonator

Mohammadreza Zamanzadeh · Hil G. E. Meijer · Hassen M. Ouakad

Received: 4 December 2021 / Accepted: 7 July 2022

Abstract In this work, we explore internal resonances in a levitation force microelectromechanical system-based actuator assuming flexible cantilever and clamped–clamped microbeam configurations. The levitation force is generated through a special arrangement of two-side stationary charged substrates and a central grounded stationary strip. The design assumes as well an upper flexible microbeam strip. The DC part of the excitation voltage pushes up the moving microbeam away from its lower stationary electrode. A superimposed harmonic AC voltage lets the flexible strip vibrate around its equilibrium position. Energy exchange among the computed lower vibration frequencies and their respective frequency and force response curves are explored for possibilities of principal parametric and internal resonances interactions. The generated responses are computed using the bifurcation toolbox MatCont. The effect of Von Karman nonlinearity to power the energy exchange within vibration modes is explored and dominant factors in the MEMS design for resonances are found from a two-parameter bifurcation analysis. Our results allow optimizing the micro-actuator device performance for future applications.

Keywords Levitation force · Internal resonance · Principal parametric resonance · Stability analysis · MatCont

M. Zamanzadeh
Mechanical Engineering Department, Urmia University, Urmia, Iran

H. G. E. Meijer
Faculty of Electrical Engineering, Mathematics and Computer Science, Applied Analysis, University of Twente, Twente, The Netherlands

H. M. Ouakad (✉)
Mechanical and Industrial Engineering Department, College of Engineering, Sultan Qaboos University, PO-Box 33, Al-Khoudh, 123, Muscat, Oman
e-mail: houakad@squ.edu.om

1 Introduction

Micro-electromechanical devices (MEMS) are used to sense and actuate on small scales in many applications. The typical capacitive MEMS structure with attractive parallel plates suffers from permanent stiction known as pull-in instability [1–4]. In contrast, the MEMS levitation force generates a repulsive force away from the substrate underneath. Together with a higher travelling range [5] and bouncing back rather than stiction (in case of probable contact) [6], the generated levitation force offers double-side tunability [7], pairability with an attractive force for liberating a stuck moving element [8] and parametric excitation to enhance the sensing and actuating features [7,9].

Recently, this new arrangement to generate levitation has been applied in various fields. For example, Pallay et al. [10] reported that the structure could act as a filter by actuating the moving beam's different modes connected with a spring. Independently, Zamanzadeh et al. [9] and Pallay et al. [11,12] elaborated on the

Published online: 13 August 2022

capability of this microstructure for pressure sensing. Numerical bifurcation analysis revealed three distinctive regions for this system bounded by different bifurcation curves [13], each with unique and intriguing features for actuation and sensing applications. In most literature on the levitation force, the reduced-order model (ROM) has been derived assuming one mode. This assumption simplifies the behavior and analysis but comes at the cost of missing higher-order system characteristics that can profoundly affect the captured dynamic behavior and lead to wrong model predictions.

Energy transfer between vibration modes is known as internal resonance. Over the last two decades, this phenomenon has gained interest due to its promising functional improvement of MEMS resonators and sensors [14,15]. Younis et al. [16] explored the prerequisites for modal interaction in the typical straight parallel plate arrangement using the method of multiple scales. Antonio et al. [17] considered stabilizing through the coupling of two modes. Ghayesh et al. [18] studied how the nonlinear modal interaction depends on the scale and curvature. Zhang et al. [19] considered internal resonances in a clamped–clamped micro-resonator in open- and closed-loop setups. They observed an alternation in internal resonance bandwidth in their experiments and then numerically validated this. Moreover, the internal resonance improved short-term frequency stabilization. Kumar et al. [20] characterized all possible internal resonances within a clamped–clamped micro-resonator by changing the external force, geometrical and material properties. They concluded that an increased excitation amplitude widens the frequency bandwidth. More recently, Ruzziconi et al. [21] experimentally and numerically analyzed the internal resonance in a MEMS CL-CL microbeam including higher-order vibration modes and found more complex dynamic behavior such as the coexistence of different attractors and a phase shift through the resonant branch.

Various researchers investigated modal interactions of arch-shaped moving units rather than of the straight moving microbeam. For example, Hajjaj et al. [22] demonstrated veering by closely tuning the first and third resonance frequencies to each other. In subsequent work [23], they demonstrated chaotic behavior of the activated internal resonance. Ouakad et al. [24] studied the effect of the initial rise and mid-plane stretching on triggering the modal energy exchange. Wang et al. [25] combined AC and DC voltages and showed hysteresis and quasi-periodic solutions arising from the three to one internal resonance.

When the ratio between the natural frequencies of two modes is close to a commensurate ratio, some of the system's nonlinearities (quadratic, cubic, or higher) become effective in coupling the respective oscillations. These then synchronize, and an internal resonance occurs [26]. Internal resonance has recently been proposed as a mechanism to neutralize the amplitude-frequency interdependence in micromechanical oscillators as that effect hinders their possible application as pacemakers in the design of time-keeping miniaturized devices. It has been applied to improve the frequency stabilization of self-sustained microresonators and compensate for energy losses [17]. Therefore, our study of internal resonances, in the end, is crucial for the successful implementation of these devices. In all of the above studies, the dynamical analyses employed higher-order modes, multiple time scales, Poincaré sections or the fast Fourier transformation (FFT) to identify the different dynamical features of the examined MEMS structure. These studies included investigating the effect of modal interactions on the dynamics of classical parallel-plates electrostatic-based design of MEMS structures. However, such investigations remain unexplored for several designs, such as the fringing-fields electrostatic-based MEMS levitation force design. Therefore, this study aims to demonstrate the possibilities of internal resonance activations among higher-order modes and characterize the dynamic behavior for MEMS levitation force-based designs. As a substitute for the typical numerical methods discussed above in the literature review, we propose using a numerical bifurcation analysis tool implemented in the MATLAB toolbox MatCont to obtain the system's periodic solutions with their respective stability status and therefore detect all possible bifurcations. The main advantage of this tool, compared to other methods, is that it deals directly with the system's equations of motion without extra approximations.

Thus, the outline of this paper is as: In Sect. 2, we specify the model and formulating the system with the nonlinear ordinary differential equations and describe how MatCont is used for our analysis. The results are presented in Sect. 3 for both the cantilever (CL) and clamped–clamped (CC) microbeams which then are compared from the stability perspective. We conclude in Sect. 4 with a summary of the necessary conditions

for the occurrence of internal resonance in MEMS with levitation force.

2 Modeling of the levitation force actuator and problem formulation

The design of the proposed repulsive force actuator consists of a suspended cantilever or clamped–clamped moving electrode, a fixed middle electrode placed directly underneath the moving one, and two side electrodes, as shown in Fig. 1.

Unlike the classical parallel plate arrangement in which the attractive force generates by applying a voltage to the moving electrode while the beneath stationary substrate is grounded, the design we explore here generates a levitation force by having the middle electrodes grounded and simultaneously charge the side electrodes, as displayed in Fig. 2a. As a result (see Fig. 2b), there is an average net upward force over the boundaries of the moving electrode, which pushes it away from the substrate underneath.

We treat the movable electrode-based actuator shown in Fig. 1 within the framework of Euler–

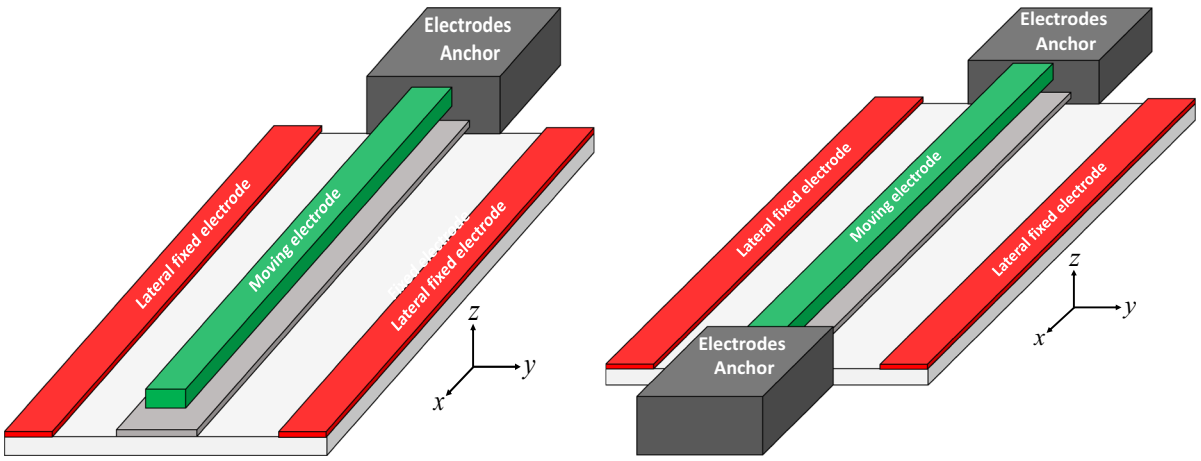

Fig. 1 3D view of the levitation force MEMS actuator in case of **a** cantilever, **b** clamped–clamped arrangements

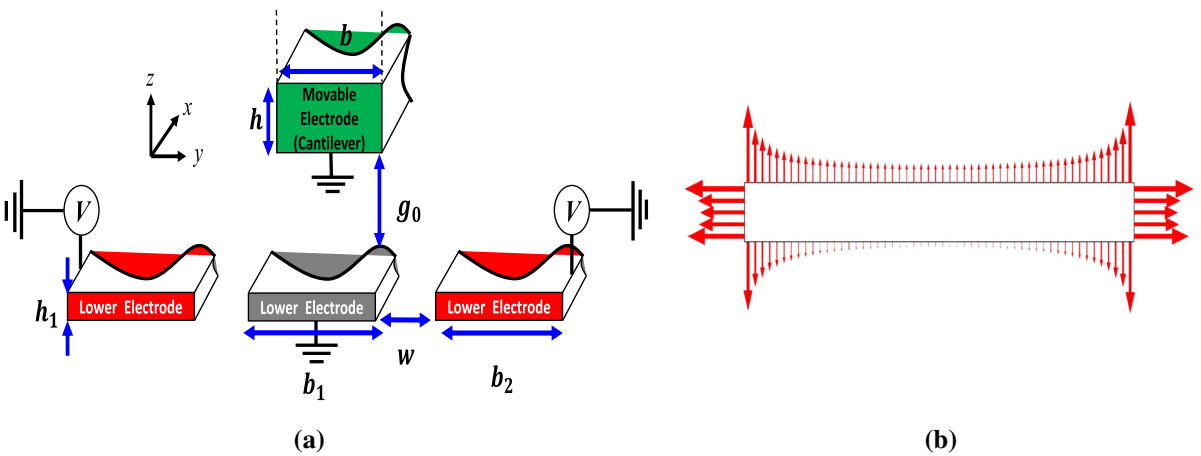

Fig. 2 **a** 2D schematic front view of the arrangement displaying the electrical and geometrical characteristics in which the side electrodes are charged and the middle ones are grounded, **b** 2D finite element simulation for electric force distribution around the boundaries of moving electrode. The upward and downward arrows represent the repulsive and attractive force, respectively

Table 1 Geometrical and material properties of the repulsive force actuator

Parameter	Symbol	value
Middle beam length (Clamped-Clamped) (μm)	L	1000
Middle beam length (Cantilever) (μm)	L	503,1000
Middle beam width (μm)	b	17.5
Grounded middle electrode width (μm)	b_1	30
Grounded side electrode width (μm)	b_2	288
Upper electrode thickness (μm)	h	2
Lower electrode thickness (μm)	h_1	0.5
Middle beam electrode gap (μm)	g_0	2
Side electrode gap (μm)	g_1	2
Lateral distance (μm)	w	20.5
Elastic modulus (Gpa)	E	150
Density (kg/m^3)	ρ	2320
Poisson's ratio	ν	0.22
Air permitivity (pF/m)	ε_0	8.854
Characteristic height (μm)	$\bar{z}$	2

Bernoulli beam theory. The actuator can freely deflect in the out-of-plane (z) direction, while its in-plane (y) deflection is negligible because of the high width-to-thickness ratio. Including the stretching effect, the corresponding normalized equation for the out-of-plane motion of the repulsive force actuator, in non-dimensionalized form, can be written as [5]:

$$\frac{\partial^2 w}{\partial t^2} + \mathcal{C}^* \frac{\partial w}{\partial t} + \frac{\partial^4 w}{\partial x^4} - r_1 \left[\int_0^1 \left(\frac{\partial w}{\partial x} \right)^2 dx \right] \frac{\partial^2 w}{\partial x^2} + r_2 V^2 f_e(w) = 0, \tag{1}$$

where the geometrical and normalizing parameters in the above equation are listed in Tables 1 and 2. For the cantilever beam the stretching effect is negligible, i.e., we set $r_1 = 0$, while for the clamped–clamped beam, we set $r_1 = 6$.

Table 2 Normalizing parameters as in [5]

Parameter	Substitution
Nondimensional length position	$x = \hat{x}/L$
Non-dimensional deflection	$w = \hat{w}/\bar{z}$
Non-dimensional time	$t = \hat{t}/T$
Non-dimensional damping	$\mathcal{C}^* = \alpha^2/\mathcal{Q}$
Area cross section(m^2)	$A = bh$
Moment of inertia(m^4)	$I = bh^3/12$
Time constant(s)	$T = \sqrt{\rho A L^4/EI}$
Mid-plane stretching constant	$r_1 = 6\left(\frac{g_0}{h}\right)^2$
Force constant(m/N)	$r_2 = L^4/EI\bar{z}$
$1st$ mode natural frequency	α
Quality factor	$\mathcal{Q}$

2.1 Reduced-order modeling

We perform a Galerkin-based reduced-order modeling (ROM) [27–29] on Eq. (1) in order to approximate the moving electrode resultant static/dynamic deflection (response) as:

$$w(x,t) = \sum_{i=1}^{N} U_i(t)\varphi_i(x) \tag{2}$$

The ROM process results in a system of coupled nonlinear and coupled ordinary differential equations in which U_i represents the generalized coordinates depending on time. The basis functions, $\varphi_i(x)$, have the following form:

$$\varphi_i(x) = \sin(\beta_n x) - \sinh(\beta_n x) - \sigma_n\left[\cos(\beta_n x) - \cosh(\beta_n x)\right] \tag{3}$$

in which β_n denotes the square roots of the non-dimensionalized natural frequencies, and σ_n are constants determined from the boundary conditions and mode to be considered (see Table 4).

To proceed, we need the distributed electrostatic force and the generated levitation force per unit length ($f_e(w)$). These data have been derived from 2D finite element simulations and then fitting the electrostatic profile to a fifth-order polynomial as done in [5], which also includes an experimental validation. We list the coefficients in Table 3. Now, the resulting system of

Table 3 Force constants defining the electrostatic force profile from [6]

Symbol	Unit	value
$\mathcal{A}_0$	N/m	-1.1703×10^{-7}
$\mathcal{A}_1$	N/m^2	-3.8677×10^{-4}
$\mathcal{A}_2$	N/m^3	3.5574×10^{2}
$\mathcal{A}_3$	N/m^4	-1.2595×10^{7}
$\mathcal{A}_4$	N/m^5	1.7347×10^{11}
$\mathcal{A}_5$	N/m^5	-8.5695×10^{14}

Table 4 Mode shape natural frequencies and constants [5]

Mode	β_n^2(CL)	σ_n(CL)	β_n^2(CC)	σ_n(CC)
1	3.516	0.7341	22.3733	0.9825
2	22.035	1.01185	61.6728	1.00078
3	61.697	0.9992	120.903	0.9999

ODEs can be written as [30]:

$$\sum_{i=1}^{N} \mathcal{M}_{ij}\ddot{U}_i(t) + \sum_{i=1}^{N} \mathcal{C}_{ij}\dot{U}_i(t) + \sum_{i=1}^{N} \mathcal{K}_{ij}U_i(t) - \sum_{i=1}^{N} \mathcal{S}_{ij}U_i^3(t) + F_j = 0, \tag{4}$$

where $\mathcal{M}, \mathcal{C}, \mathcal{K}$ and $\mathcal{S}$ are mass, damping, mechanical stiffness and stretching matrices, respectively, and F stands for the forcing vector. They are defined by:

$$\begin{aligned}
\mathcal{M}_{ij} &= \int_0^1 \varphi_i \varphi_j dx \\
\mathcal{C}_{ij} &= \mathcal{C}^* \mathcal{M}_{ij} \\
\mathcal{K}_{ij} &= \int_0^1 \frac{d^2\varphi_i}{dx^2}\frac{d^2\varphi_j}{dx^2} dx \\
\mathcal{S}_{ij} &= r_1 \left[\int_0^1 \left(\frac{d\varphi_i}{dx}\right)^2 dx\right] \int_0^1 \varphi_j \frac{d^2\varphi_i}{dx^2} dx \\
F_j &= r_2 V^2 \int_0^1 \sum_{k=0}^{5} \mathcal{A}_k \bar{x}^k \left(\sum_{i=1}^{N} U_i \varphi_i\right)^k \varphi_j dx
\end{aligned} \tag{5}$$

2.2 Dynamic response evaluation using numerical continuation

Here we outline our numerical approach to obtain the dynamic response of the repulsive electric micro-actuator. The objective is to obtain the frequency-response as the beam is deflected by a DC voltage and vibrates by an AC harmonic load with a frequency near the intrinsic frequency. One can use time integration, but this method suffers from slow convergence to an attractor, convergence problems near bifurcations, and one cannot identify unstable solutions. In addition, methods such as shooting are highly sensitive to the initial conditions to find the response, especially near bifurcations.

These considerations motivate us to use numerical continuation with MatCont [31,32] to compute one-parameter families (branches) of periodic orbits. MatCont computes a limit cycle (isolated periodic orbit) using a boundary-value problem. The time interval is rescaled to [0,1] and discretized into short intervals. The period is then included in the unknown quantities. The orbit is approximated by a polynomial satisfying the nonlinear system on each short time interval. The final and initial state variables of two subsequent intervals should be the same, and for periodicity, the final and initial points of the whole mesh are also required to be the same. A phase condition guarantees the uniqueness of the resulting nonlinear system, which are solved with Newton iterations. Adding a pseudo-arclength condition, we can use numerical continuation to explore the parameter dependence of the periodic orbit.

This approach also provides the Floquet multipliers to determine the stability of the periodic orbit as a function of the parameter, e.g., the forcing frequency. When the stability changes, we find codimension-one bifurcations. Freeing one more parameter, we can compute bifurcation curves in the parameter plane. MatCont assumes an autonomous first-order system. To this end, we first reformulate the system of second-order ODEs (5) as a first-order system. To arrive at an autonomous system, we augment the system with two ODEs for the periodic forcing.

$$\begin{cases} X' = -\omega Y + X(1 - X^2 - Y^2), \\ Y' = \omega X + Y(1 - X^2 - Y^2). \end{cases} \tag{6}$$

These equations come from the normal form for the Hopf bifurcation. It is easy to see that X and Y evolve on the unit circle. We can now replace any term such as $cos(\omega t)$ by X. Next, we initialize the system with $X = 0$ and $Y = 1$ and $U_i = U_i' = 0$ and perform time-integration until transients have faded and the state converged to the steady-state response. We then pick up the

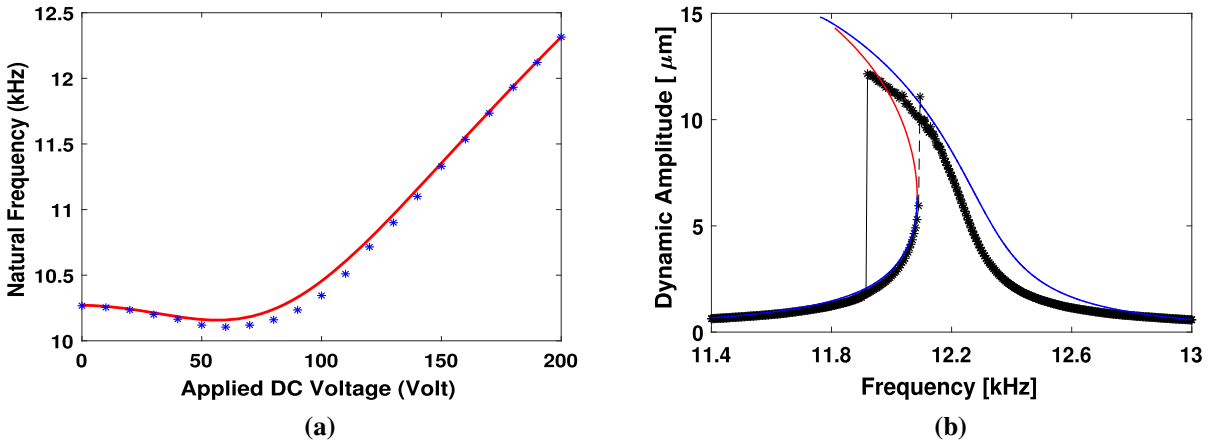

Fig. 3 Comparison of the numerical (solid line) and experimental (dots) results for **a** first natural frequency (experimental results obtained from (data adapted from [5]) and **b** dynamical response (experimental results obtained from (data adapted from [30])

final point of this simulation and perform one more time integration for one forcing period. This last simulation is used as initial data for the numerical continuation. For the continuation, we select the forcing frequency Ω and the period as free parameters. The continuation produces a sequence of points with an approximation of the periodic response for each parameter value. We plot the maximal amplitude of the variable U_1 as a function of the forcing frequency Ω. For terminology about bifurcations, we refer to [32].

3 Results and discussion

3.1 Initial exploration for internal resonance

The essential condition for internal resonance is that one natural frequency is an integer multiple of another. One can obtain the natural frequencies from the eigenvalues of the Jacobian matrix of Eq. 4 by excluding the damping term and evaluating at the fixed point, i.e., the static equilibrium [33]. Before starting the analysis, one needs to validate the governing equation of motion with some available experimental results. In Fig. 3, we show the first natural frequency as a function of the applied DC voltages as determined experimentally in [5] and as reported for the dynamical response in [30]. We observe close agreement in Fig.3a in which the frequency exhibits a falling-rising pattern with a minimum as the DC voltage increases. This minimum comes from the repulsive force and is critical for tuning the system. Moreover, Pallay et al. [5] attributed the observed slight difference to the dimples placed in the tested system to prevent the stiction. The dynamic response in Fig.3b has a slightly larger discrepancy. This discrepancy is already addressed and well justified by Dr. Towighian and her research team during their evaluations. It is mainly attributed to the additional Squeeze Film Damping which adds extra stiffness beneath the resonant micro-beam, which, specifically in the resonant region, acts as a damper adding rigidity to the system. During the experiment they observed that, the moving micro-beam cannot freely vibrate, and an additional damping term should be added to account for the damping properly [6,11]. However, here we focus on the possibility of the internal resonance in the studied MEMS device rather than pinpointing the exact location of the resonant beam.

The numerical and experimental data fit the first natural frequency well. Therefore, we assume that the numerical approach can also predict higher-order natural frequencies with similar accuracy although the dynamic response does not hold such precision. Some modes contribute little due to the geometry of the system and boundary conditions of the moving element. Therefore, we include the second mode for the CL case and up to the third mode for the CC case.

The length of the moving micro-beam is a crucial parameter dominating the systems' response. Along with the alternation in moving stroke of the system, the length affects the natural frequencies, the commensurate threshold of the applied DC voltage and consequently the ratio of the frequencies. For the latter,

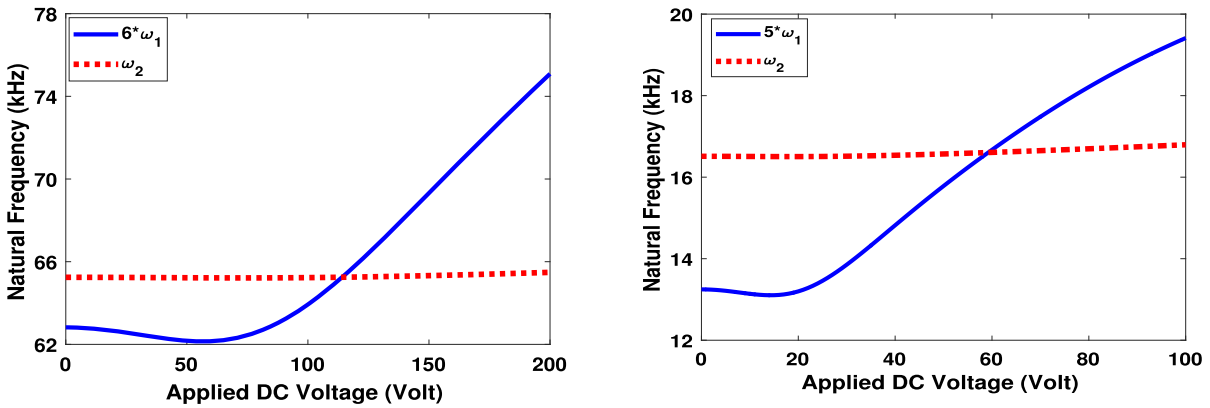

Fig. 4 Exploring ratios of the natural frequencies for first and second mode for the cantilever microbeam with **a** $L = 503\,\mu m$ and **b** $L = 1000\,\mu m$

we plot integer multiples of the natural frequencies for the cantilever microbeam with $L = 503$ and $L = 1000$ microns to observe crossings, as in Fig. 4. These graphs suggest that increasing the beam length lowers the ratio of the frequencies and also the activation threshold of the applied DC voltage. However, this initial sign of internal energy exchange must still be validated by assessing the nonlinear dynamical response.

Similarly, in Fig. 5 we show the corresponding diagram for the CC microbeam. We observe that the first and third natural frequencies exhibit a three to one internal resonance. As this ratio is of lower order in comparison with the cantilever case (Fig. 4), this CC case is more likely to enable energy exchange between the vibration modes.

The approach, as shown in Figs.4 and 5, highlights how shapes and boundary conditions lead to the quantitative and qualitative alternation in natural frequencies. Similarly, we can also explore how the von Karman nonlinearity, standing as the stretching term in the clamped–clamped micro-beam, influences the possibilities of internal resonance. We recompute the first and third mode frequencies for the CC micro-beam, where we now neglect the stretching term by setting $r_1 = 0$, see Fig. 6. We observe that the frequencies are of a different order and commensurate by a much bigger integer. The higher proportional integer between the mode frequencies minimizes the power of energy exchange between modes. Comparing with Fig. 5, where we included the stretching term, we conclude that the von Karman nonlinearity rather than the repulsive force is the pivotal term for energy exchange across modes, albeit the repulsive force undergoes changes to the interacted modal system via the stretching term.

Having determined the natural frequencies, we can now fix the applied DC voltage in the range where the static analysis foretells internal resonances. Next, we investigate the effect of the excitation voltage (V_{AC}) and frequency (Ω) on the frequency response and possible energy exchange. Here we note that in order to prevent the moving element from hitting the substrate, the applied AC voltage is tuned so that the applied bias DC voltage is much higher than applied AC voltage ($V_{DC} \gg V_{AC}$). Hence, in the theoretical evaluation,

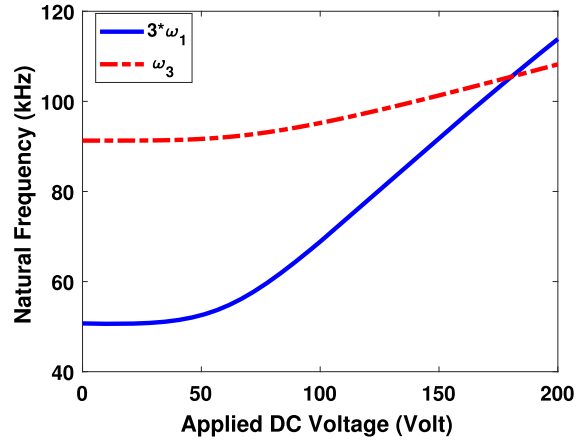

Fig. 5 Integer multiples of the first and third natural frequencies as a function of the applied DC voltage for the CC microbeam

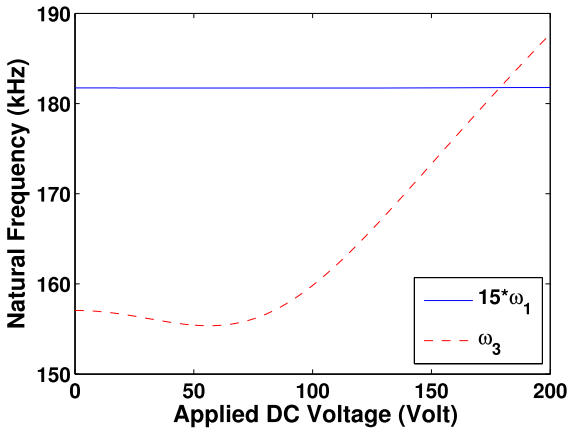

Fig. 6 Integer multiples of the first and third natural frequencies as a function of the applied DC voltage for the CC microbeam in case of excluding the stretching term

we can ignore the term related to the higher order of applied AC voltage.

3.2 Dynamic response

We determine the frequency response curves for both the CL and CC cases separately. We aim to trace the footprint of internal energy exchange. The periodic forcing leads to a periodic response by the system. In that sense, the solutions are periodic over time. The bifurcations of the periodic solutions (also referred to as limit cycles) that may occur are limit point of cycles (saddle-node), period-doubling and Neimark-Sacker. The first involves the (dis)-appearance of periodic solutions, the second leads to doubling and the third may involve multi-frequency oscillations. For more details, we refer to [34].

3.2.1 Primary internal resonance with cantilever (CL) microbeam

Guided by Fig. 4a, we first apply a DC voltage slightly higher than the predicted threshold of 115 V and fix the applied AC voltage. Next, we compute the frequency response shown for $V_{\mathrm{DC}} = 120\,V$ and $V_{\mathrm{AC}} = 0.5\,V$, see Fig. 7. The solid and dashed lines indicate stable and unstable periodic response solutions, respectively, also in the following figures. We detect no internal resonance, although the system undergoes softening tendency, which is attributed to the existence of the quadratic and negative cubic nonlinearity in the forcing term [30]. In this case, due to the negligible amplitude of the second mode, the dominant amplitude is the first mode, and the system does not exhibit any internal resonance.

To explore the effect of applied DC and AC voltage to activate the internal resonance in our case, we increase V_{DC} from 120 to 130 V and V_{AC} from 0.5 to 1.5 V. As shown in Fig. 8, despite the increase in applied voltages, the system experiences no internal resonance, but it injects energy causing additional peaks to the response of the second mode. Quantitatively, we see the amplitude increases due to the increase in DC voltage, and the peak in the amplitude response shifts with a more pronounced softening effect on the response. Moreover, it causes more prolonged

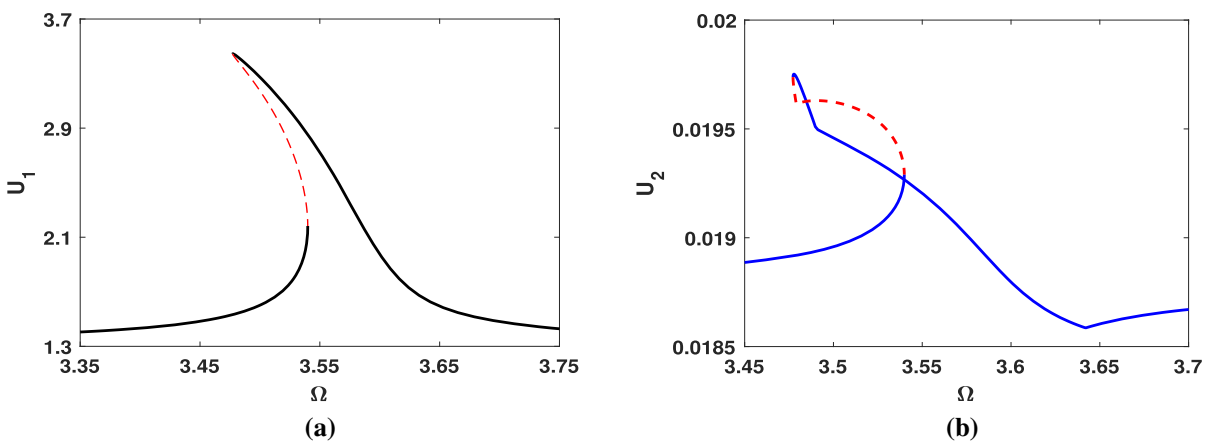

Fig. 7 Frequency response at $V_{\mathrm{DC}} = 120\,V$, $V_{\mathrm{AC}} = 0.5\,V$ for the **a** first and **b** second modes for the CL case

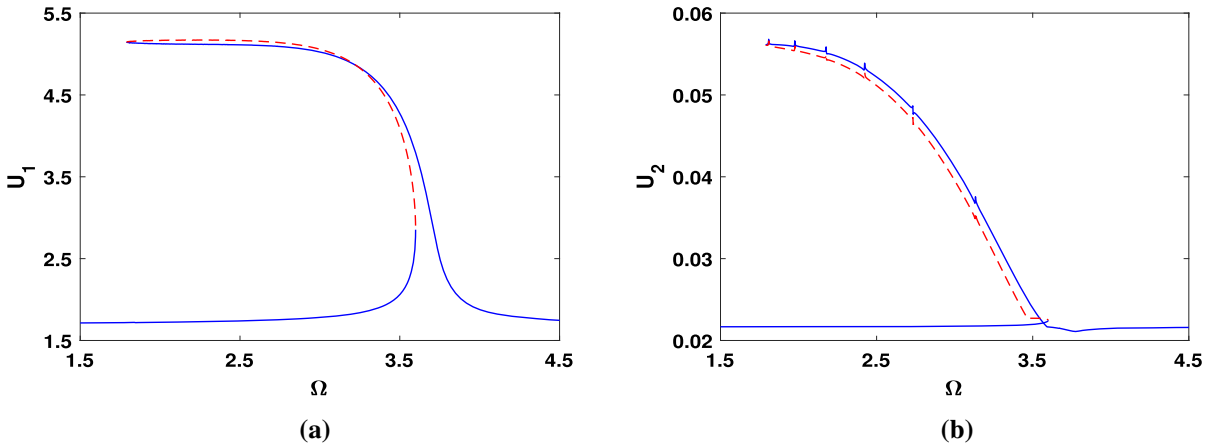

Fig. 8 Frequency response at $V_{\mathrm{DC}} = 130\,V$, $V_{\mathrm{AC}} = 1.5\,V$ for the **a** first and **b** second modes for the CL case

transients, i.e., the response takes longer to reach the periodic response.

We also determined the fast Fourier transformation (FFT) for each mode, see Fig. 9. Comparing the respective power, we see that the second mode hardly contributes. This is additional numerical evidence that energy exchange does not happen and that the first mode is the dominant mode of the system. This justifies the assumption to describe the dynamic behavior of the system with just one mode.

Although the analysis above rejects the possibility of internal resonance for the case of the CL microbeam with $L = 503$ micron, it does not remove the possibility of energy exchange between the modes completely. One key parameter here is the dimension of the moving microbeam that changes the characteristics of our system like the natural frequency, and it also decreases the stiffness of our system. Based on Fig. 4(b) for $L = 1000$ micron, we now set the DC voltage a bit beyond $V_{\mathrm{DC}} = 60\,V$, where we expect the occurrence of the five to one resonance. We computed the frequency response curve to check for internal resonances for this setting, see Fig. 10. There is a small sign of an internal resonance with as the inset shows. Here the amplitude of U_1 drops, while that of U_2 increases. The latter is smaller but still alters the behavior of the system. Below, to see the interplay of the applied voltages and forcing frequency, we will determine how the saddle-node bifurcation point M_p varies in two parameters, but first, we look at other parameter variations.

As before, we plot the corresponding time series and FFT diagram in Fig. 11. Similar to Fig. 10, the FFT results indicate again that the magnitude of the second mode is lower compared to the first mode. Still, it is large enough to alter the system's response at excitation frequencies approaching the primary resonance.

The applied AC voltage is a key parameter of the applied force affecting the system's overall response. The dependence of the amplitude on the applied AC voltage for several values of the applied frequency is illustrated in Fig. 12.

Having found the saddle-node bifurcation point M_p in Fig. 10, we now determine how this point varies in the two-dimensional parameter space $(\Omega, V_{\mathrm{AC}})$. MatCont allows computing such a branch of saddle-node bifurcation curve. Here we keep V_{DC} fixed and vary Ω and V_{AC}. We compute these curves for both the model with just one mode and the model including higher modes indicated by dashed and solid lines, respectively, in Fig. 13a. We observe that the result for more modes differs quite a bit compared to the single-mode case. Figure 13b illustrates that for increasing values of the voltages V_{DC} and V_{AC}, the Neimark-Sacker bifurcation curve leads to multi-frequency oscillations. This bifurcation curve yields a complex region near the internal resonance due to the presence of several codimension two bifurcations.

The results in Fig. 13 predict that we should have more interesting behavior when we increase the applied AC voltage. Setting $V_{\mathrm{AC}} = 0.8\,V$, through frequency responses we find out that the energy exchange between modes is larger, see Fig. 14. In addition, the resonance bends to lower frequencies with an additional drop in

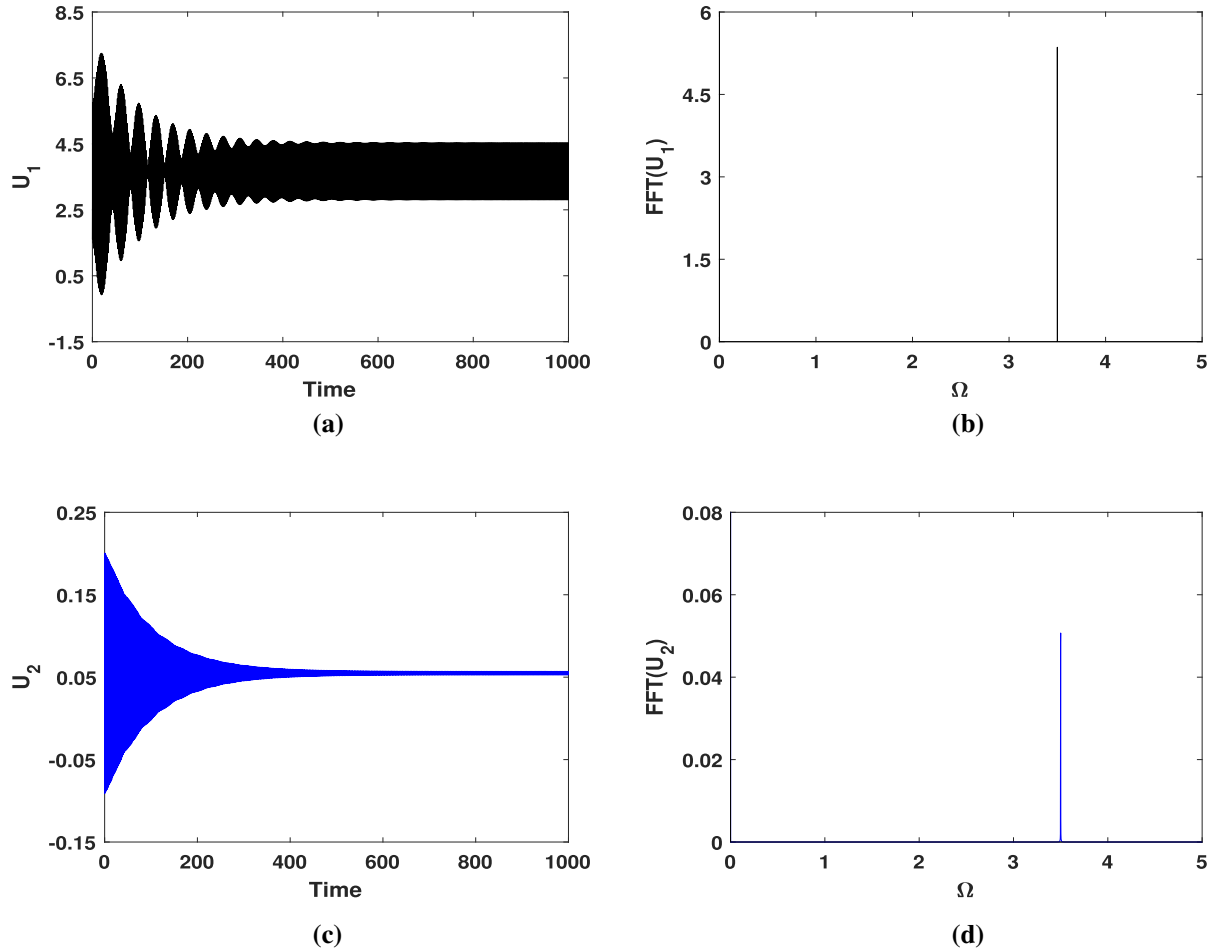

Fig. 9 **a**, **c** Amplitude response of the first and second modes for $\Omega = 3$,close to the primary resonance, **b**, **d** fast Fourier transformation (FFT) of the first and second modes, respectively, at $V_{\mathrm{DC}} = 120\,V$, $V_{\mathrm{AC}} = 1.5V$

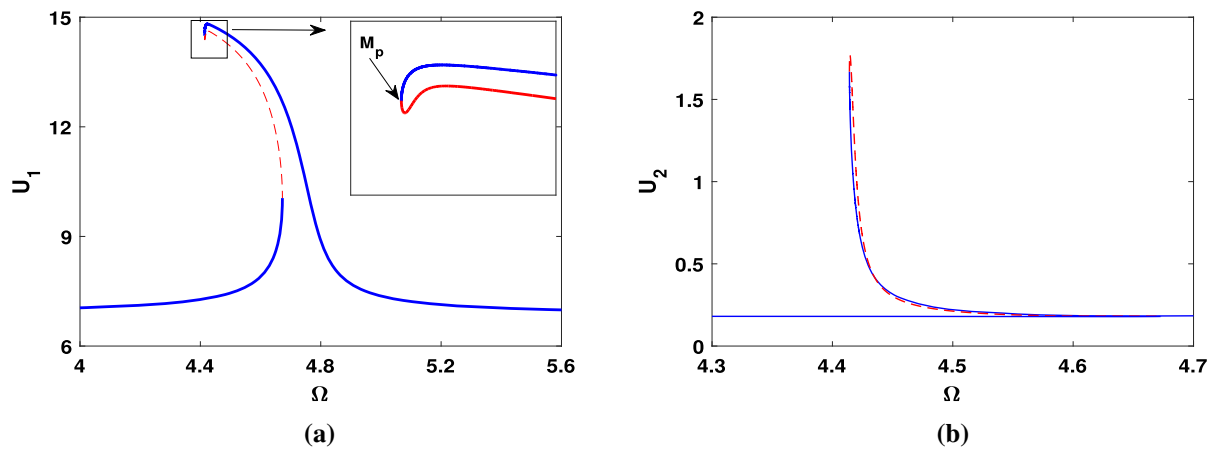

Fig. 10 Frequency response at $V_{\mathrm{DC}} = 75\,V$, $V_{\mathrm{AC}} = 0.6\,V$ for the **a** first and **b** second modes

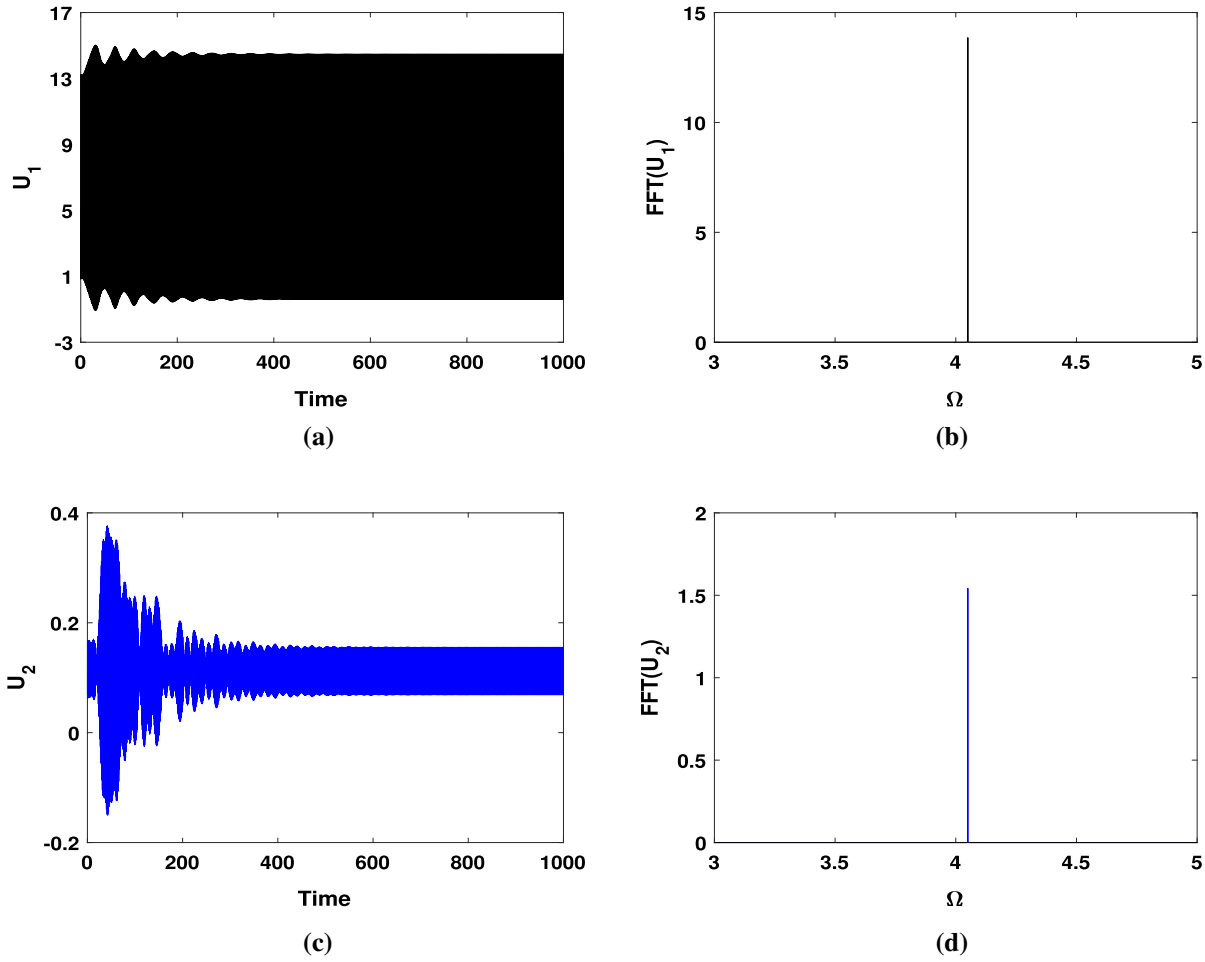

Fig. 11 **a**,**c**Time response for the amplitude of first and second modes at $\Omega = 3$, **b**,**d** fast Fourier transformation (FFT) of first and second modes, respectively, at $V_{\mathrm{DC}} = 75V$, $V_{\mathrm{AC}} = 0.6\,V$

amplitude. More of such drops in amplitude appear by increasing V_{AC}.

3.2.2 Primary internal resonance with clamped–clamped (CC) micro-beam

Here we consider the possibility of energy exchange between first and third modes through three-in-one internal resonance. Based on Fig. 6, we should explore the constant DC voltage beyond $180V$. To start, we present the frequency response at $V_{\mathrm{DC}} = 185\,V$, $V_{\mathrm{AC}} = 0.1\,V$ in Fig. 15, with a close-up for the first and third vibration modes. The figure shows how an internal resonance is springing out, even if it is small here. The amplitude of the second mode is so low that it is excluded from the analysis.

The effect of increasing the applied DC voltage while fixing the applied AC voltage is demonstrated in Fig. 16. It is intriguing to observe that for $V_{\mathrm{DC}} = 195\,V$, the double-tangled resonance vanishes as the dominant peak shrinks, and the resonance comes purely from the modal interaction. To achieve the maximal amplitude for a resonator application, the optimized range of applied DC voltage in the context of applied $V_{\mathrm{AC}} = 0.1\,V$ is near $V_{\mathrm{DC}} = 192\,V$.

To illustrate the effect of the amplitude of the alternating voltage V_{AC}, we computed the frequency response of the system for fixed $V_{\mathrm{DC}} = 195\,V$ and two different values of V_{AC} in Fig. 17. The diagram indicates the threshold for activation of the internal resonance for a fixed DC voltage. At an AC voltage of $0.1\,V$, the system's behavior has a hardening behavior.

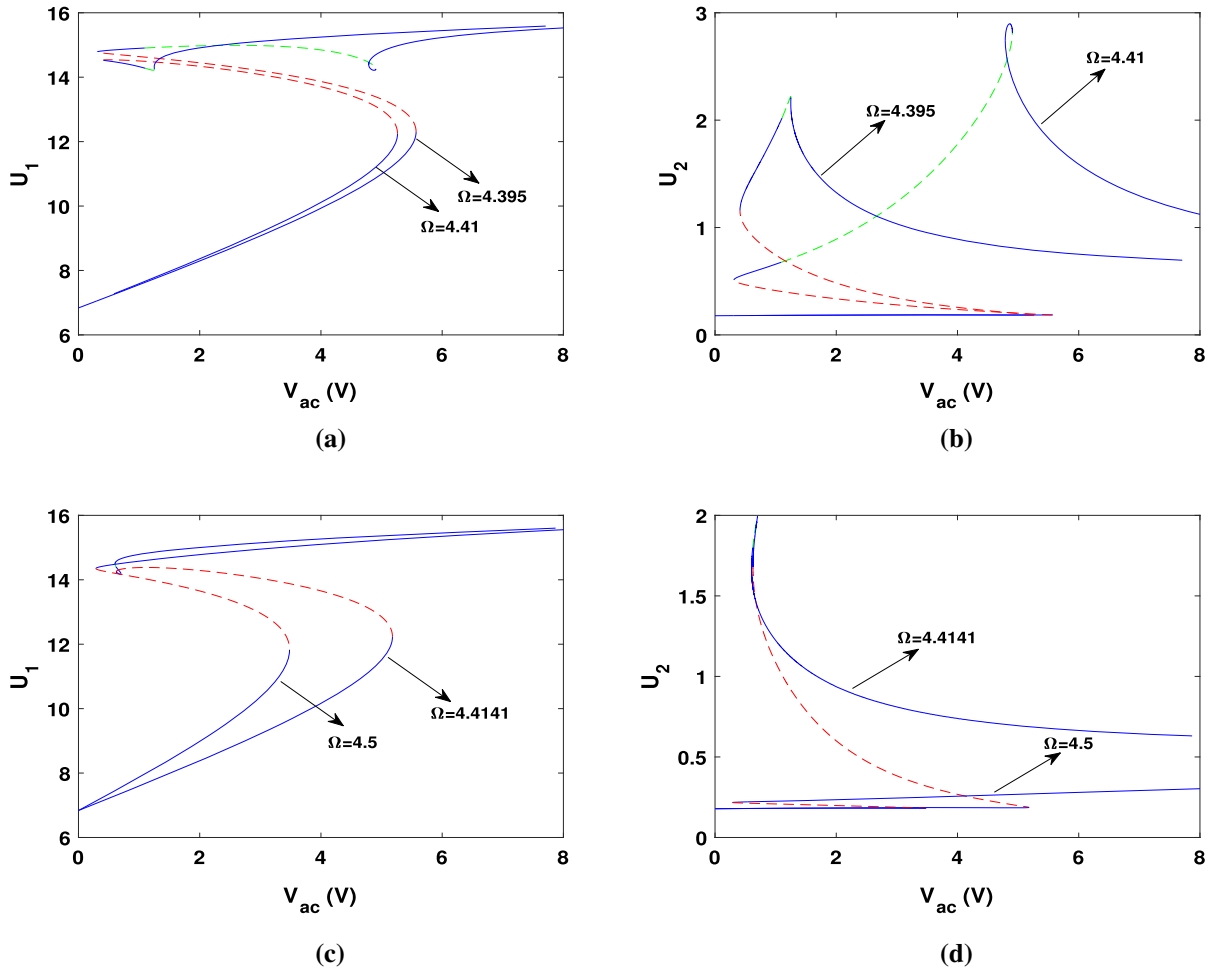

Fig. 12 Variation of force response at $V_{\mathrm{DC}} = 75\ V$ for the **a**), c first and **b**, **d** second modes

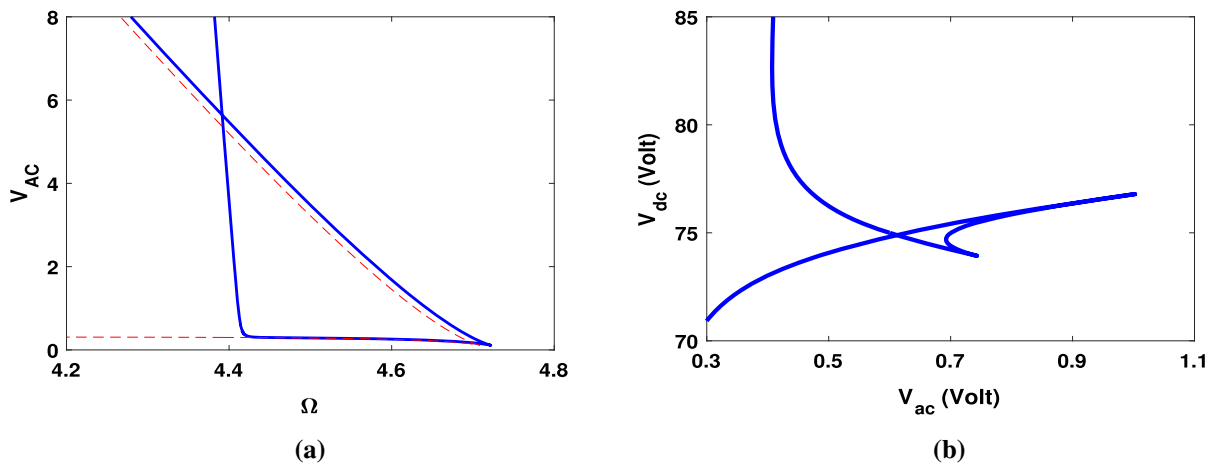

Fig. 13 Combined evaluation of the dynamic characteristic for point M_p in Fig. 10 for **a** Fixed $V_{\mathrm{DC}} = 75\ V$ with one mode and two mode in dashed and solid line, respectively, and (b) Saddle-node bifurcation in the (V_{AC}, V_{DC})-plane for fixed $\Omega = 4.4141$

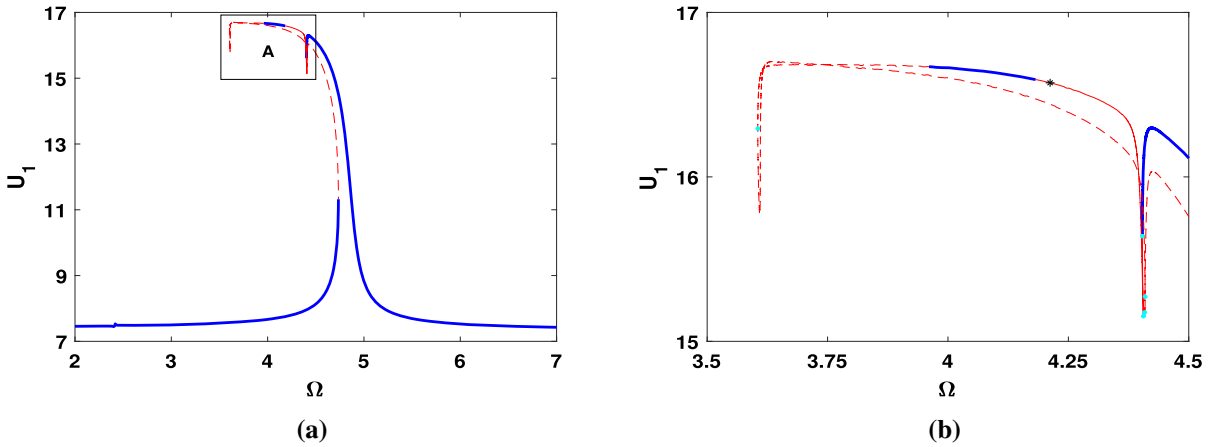

Fig. 14 Frequency response at $V_{DC} = 90\,V$, $V_{AC} = 0.8\,V$ for the first mode **a** for general Ω and **b** a close-up of region A in Fig. 14a

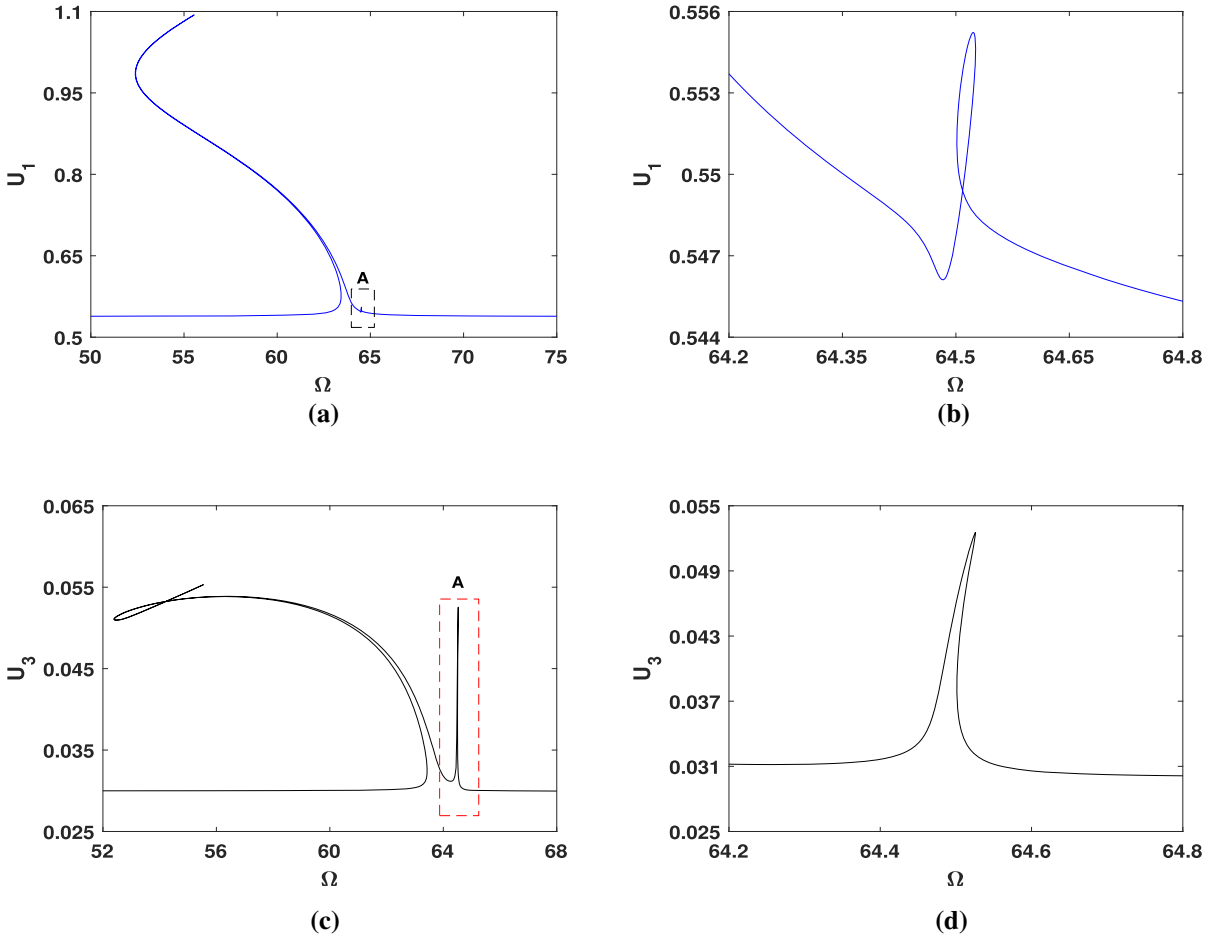

Fig. 15 **a**, **c** Frequency response of the first and third vibration modes at $V_{DC} = 185\,V$ and $V_{AC} = 0.1\,V$. **b**, **d** the zoomed-in region for frequency response of first and third modes

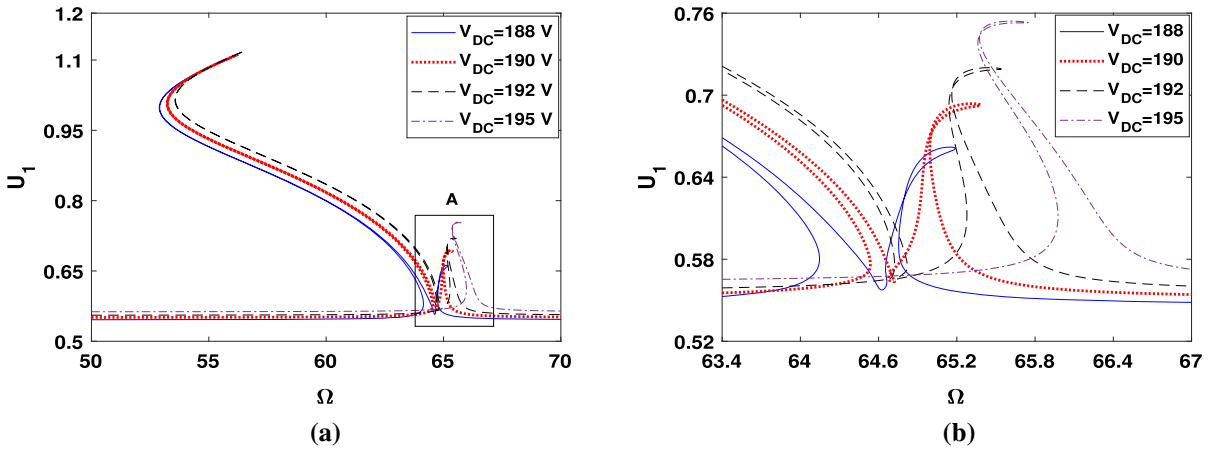

Fig. 16 **a** Comparison of the frequency response for different applied DC voltages and fixed $V_{\mathrm{AC}} = 0.1\ V$. **b** Magnification of region A near the internal resonance region in Fig. 16**a**

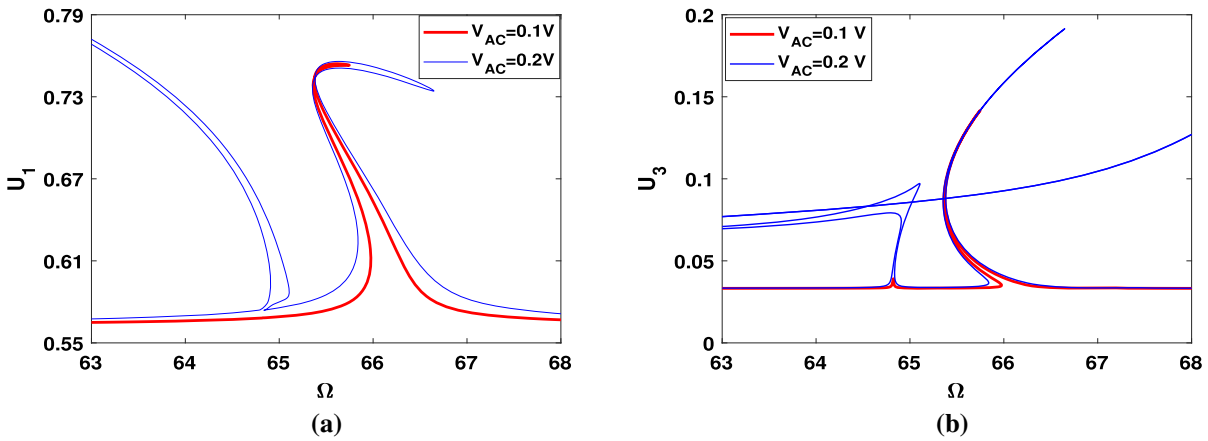

Fig. 17 Comparison of the frequency response for different applied AC voltages and fixed $V_{\mathrm{DC}} = 195$ for the **a** first and **b** third mode

Increasing the AC voltage triggers the internal resonance and leads to an additional softening behavior in the vicinity of the core hardening tendency.

To investigate the effect of increasing the applied DC and AC voltages on the nature and strength of internal resonance, we determined the frequency response for the first three modes (see Fig. 18). Comparing the results, depicted in Fig. 15, implies an expanding effect of both the AC and DC voltage. Moreover, compared to the previous figure, increasing the applied AC voltage reveals the branches switched position before exhibiting the highest response. The sub-Figs. 18b, c and d show more details of the response and indicate some crucial points. Here LPC stands for saddle-node of periodic orbits while NS represents Neimark-Sacker of periodic orbits leading to a torus with multi-frequency responses. To study the behavior near the Neimark-Sacker bifurcation, we pick a bifurcation point NS and label it as M_p for monitoring and further evaluation.

To cast light on the effect of stretching term and its importance in the energy exchange within the vibration modes, Fig. 19 illustrates the frequency response for systems parameters similar to Fig. 18. Comparing the latter diagrams shows how neglecting the stretching term leads to a rise in the amplitude but ruins the possibility of modal interaction. Furthermore, similar to Fig. 6, it illustrates that the higher value of the proportionate integer makes the energy exchange too weak to affect the dynamical response.

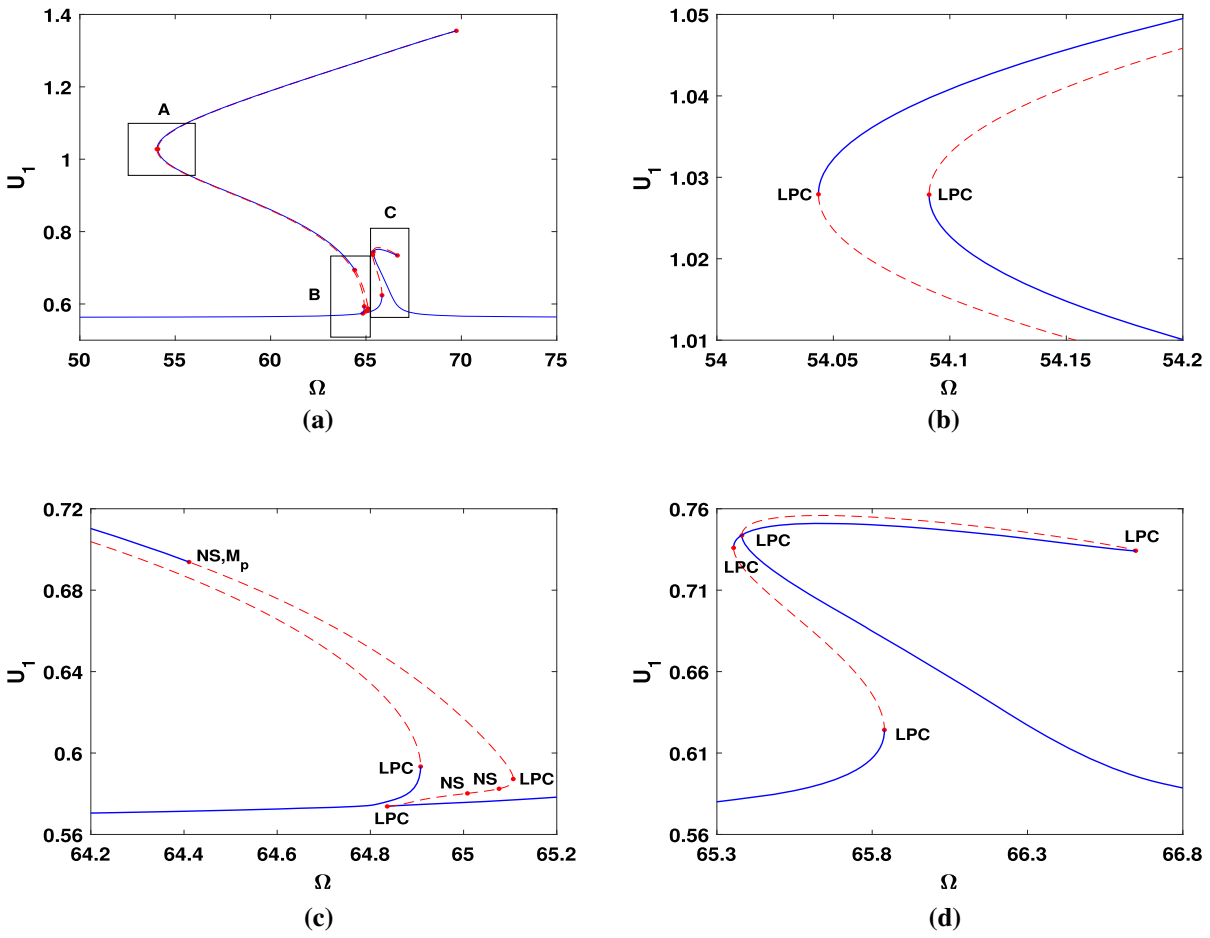

Fig. 18 **a** Frequency response of the first vibration mode at $V_{\mathrm{DC}} = 195\ V$ and $V_{\mathrm{AC}} = 0.2\ V$, **b** zoom-in region A, **c** zoom-in region B, **d** zoom-in region C

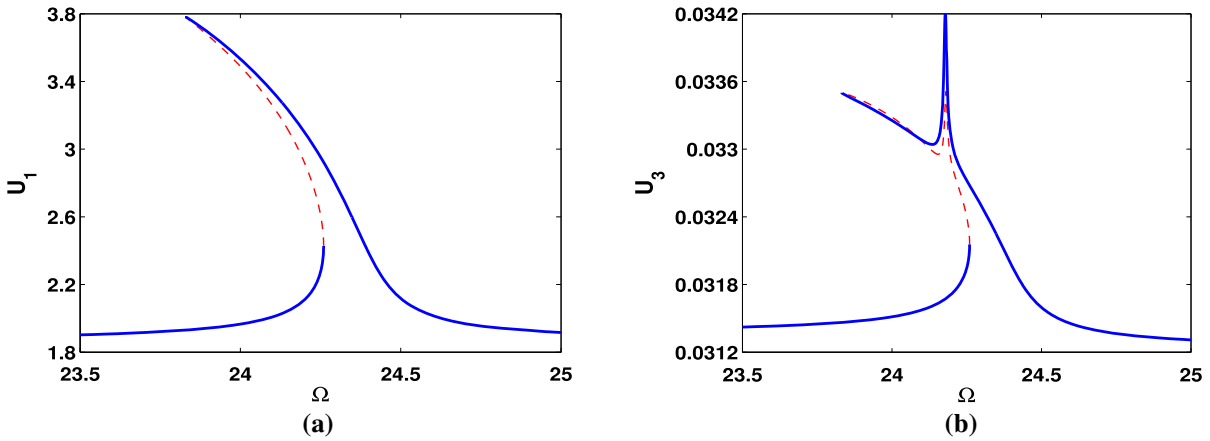

Fig. 19 Frequency response of CC micro-beam by removing the stretching term at $V_{\mathrm{DC}} = 195\ V$ and $V_{\mathrm{AC}} = 0.2\ V$ for the **a** first and **b** third mode

To cast light on the effect of stretching term and its importance in the energy exchange within the vibration modes, Fig. 19 illustrates the frequency response under systems parameters similar to Fig. 18. Comparing the latter diagrams implies that how neglecting the stretching term brings about a rise in the amplitude but ruins the possibility of modal interaction. Furthermore, it further validates the deduced implication coming from Fig. 6 in which the much higher value of proportional integer makes the energy exchange too week to affect the dynamical response.

Following the Neimark-Sacker bifurcation in two parameters, we find several codimension two bifurcations as shown in Fig. 20. We first vary the applied DC voltage and the applied frequency keeping the applied AC voltage fixed in Fig. 20a, and next, we vary the applied AC voltage and the applied frequency while keeping the applied DC voltage constant in Fig. 20b. Here many fascinating points arise, wherein dots stand for primary resonance, stars represent Chenciner (degenerate NS) bifurcation, and squares indicates double Neimark-sacker.

To detect the effect of AC voltage on the higher applied DC voltages, Fig. 21 illuminates the frequency response for $V_{\mathrm{DC}} = 200\,V$ and various AC voltages. Compared to the previous figure (see Fig. 17), we see that the increasing V_{AC} no longer provides the highest branching, albeit results in a tiny rising/falling response. The dots in the sub-Figs. 21c and d stand for limit point cycle.

In Fig. 21, we observe two separate regions with higher response amplitude. To provide a better understanding, we show the response in the vicinity of region A in Fig. 21a against increased applied AC voltage in Fig. 22. In the figures, dots and start indicate limit-point-of-cycles and Neimark-Sacker bifurcations, respectively.

Similar to the later figure, Fig. 23 depicts the force response for the main region with highest response represented in Fig. 21a by defining the critical points in dots and starts as well as stable and unstable responses in solid and dashed lines, respectively.

3.2.3 Principle parametric internal resonance

The feasibility of combined internal resonance in the presence of principal parametric resonance has been already investigated for an axially moving beam with simple support [35,36] and a hinged-clamped uniform prismatic beam [37]. For the levitation force MEMS device, only the principal parametric resonance was derived and validated experimentally [6,38]. However, here we explore the modal interaction and dynamical effect of the resonance at the principal parametric response for the first time within this repulsive configuration by modulating the excitation frequency in the vicinity of twice the primary resonance. We benefit from using MatCont as period-doubling bifurcations are readily detected and can be used to start branches with twice the period [31].

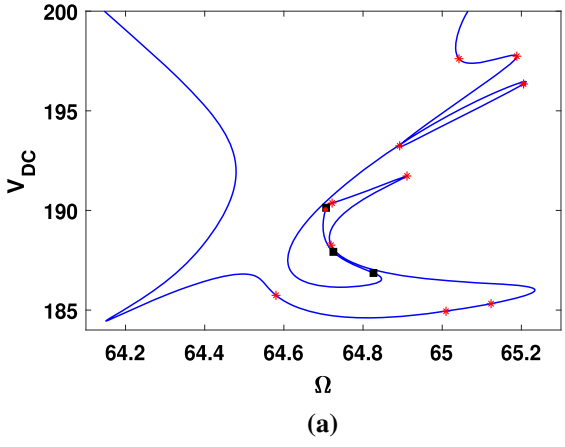

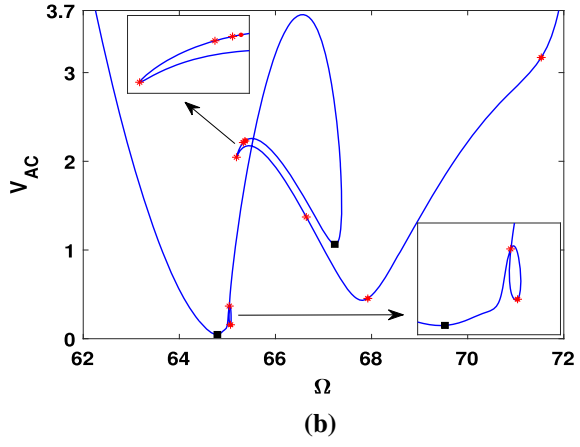

Fig. 20 Continuation of the Neimark-sacker bifurcation in two parameters starting from M_p in Fig. 18c with **a** fixed AC voltage and **b** fixed DC voltage wherein dots,stars and squares represent primary resonance, Chenciner (degenerate NS) bifurcation, and double Neimark-sacker, respectively

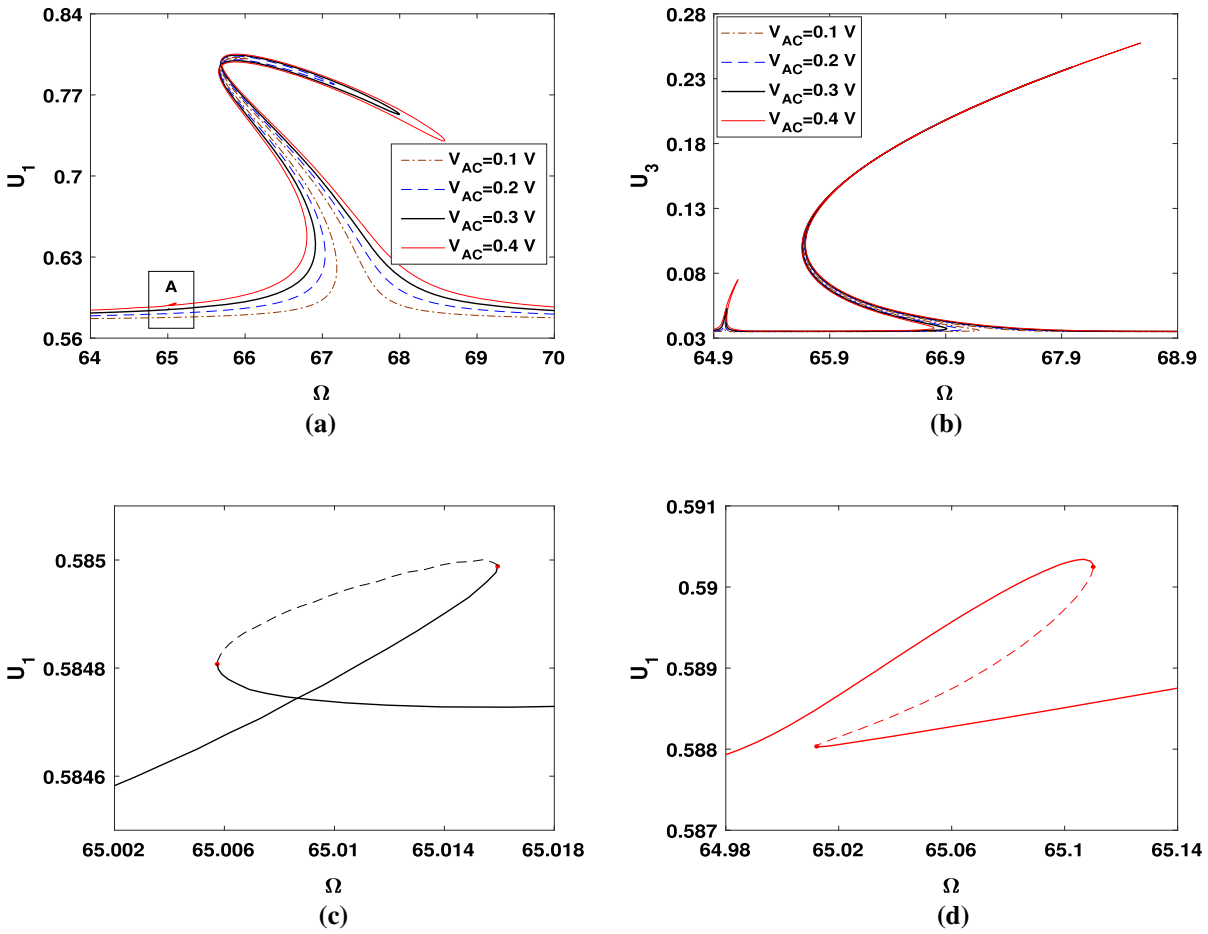

Fig. 21 A comparison of the frequency response for different applied AC voltages and fixed $V_{\mathrm{DC}} = 200$ **a** for the first mode ,**b** for the third mode,**c** closed view of region A in Fig. 21a for $V_{\mathrm{AC}} = 0.3\,V$, d closed view of region A in Fig. 21a for $V_{\mathrm{AC}} = 0.4\,V$

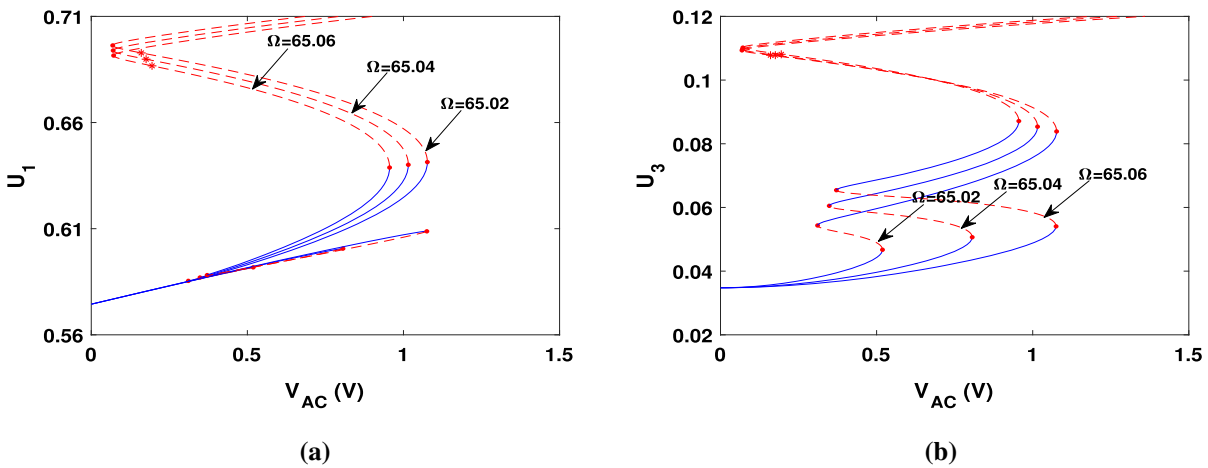

Fig. 22 Force response in the vicinity of region A in Figure 21a for the **a** first vibration mode,**b** third vibration mode

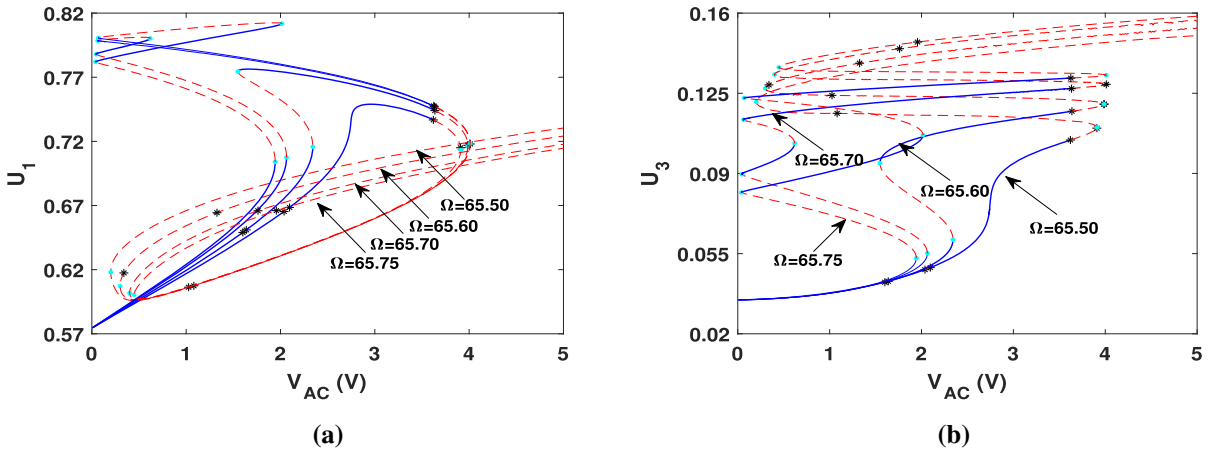

Fig. 23 Force response in the vicinity of region *A* in Fig. 21a for the **a** first and **b** third vibration mode

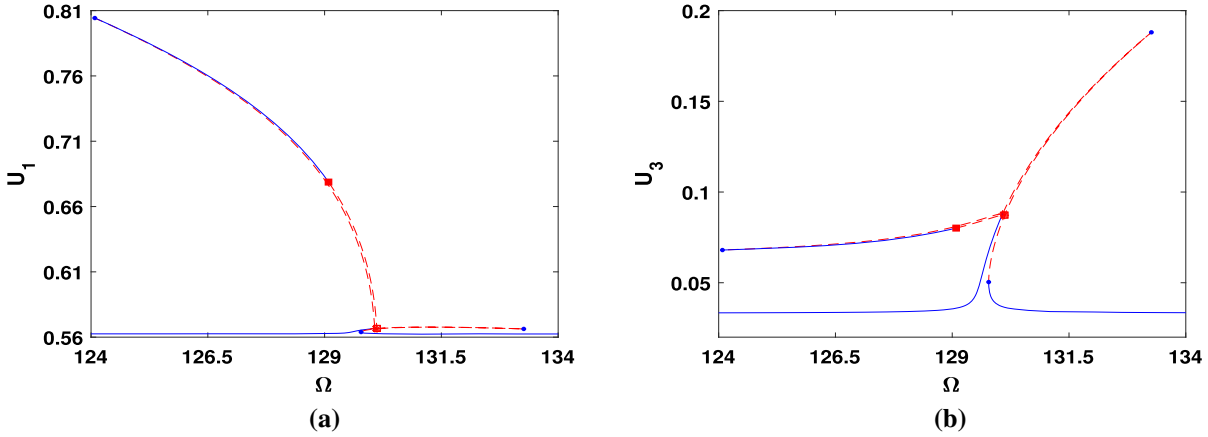

Fig. 24 Force response in the vicinity of principle parametric resonance at $V_{\mathrm{DC}} = 195\,V$ and $V_{\mathrm{AC}} = 0.1\,V$ for the **a** first vibration mode, **b** third vibration mode

For the microstructure with CC moving element, to compare the results with those in the vicinity of the primary resonance, we start our exploration of the frequency response by setting $V_{\mathrm{DC}} = 195\,V$ and $V_{\mathrm{AC}} = 0.1\,V$. The results are shown in Fig. 24.

Comparing the latter figure with the corresponding plot of the primary resonance (see Fig. 17a) shows that the system can produce higher stroke in the case of principal parametric resonance thanks to the energy exchange between the vibration modes. This is a crucial feature due to the higher-order mode, which significantly improves the structure's performance by an additional rising response with the magnitude of a third of the primary response. Furthermore, the branching happens around $\Omega = 130$. The effect of a higher applied AC voltage is illuminated in Fig. 25, where, in comparison with Fig. 18, the system generates a lower maximum amplitude albeit with additional rising response compared to Fig. 24. This provides an enhancement for functional application of the element in sensing/actuating purposes. In the sub-figures, we present a magnification near the bifurcation points by highlighting the important points where limit point cycles are indicated by dots and stars stand for period-doubling bifurcations.

To observe the effect of increasing the applied AC voltage, we plot the force response within some important applied frequency next to the branching region in Fig. 26. Here stars stand for period-doubling, dots represent limit point cycles, and squares mark the

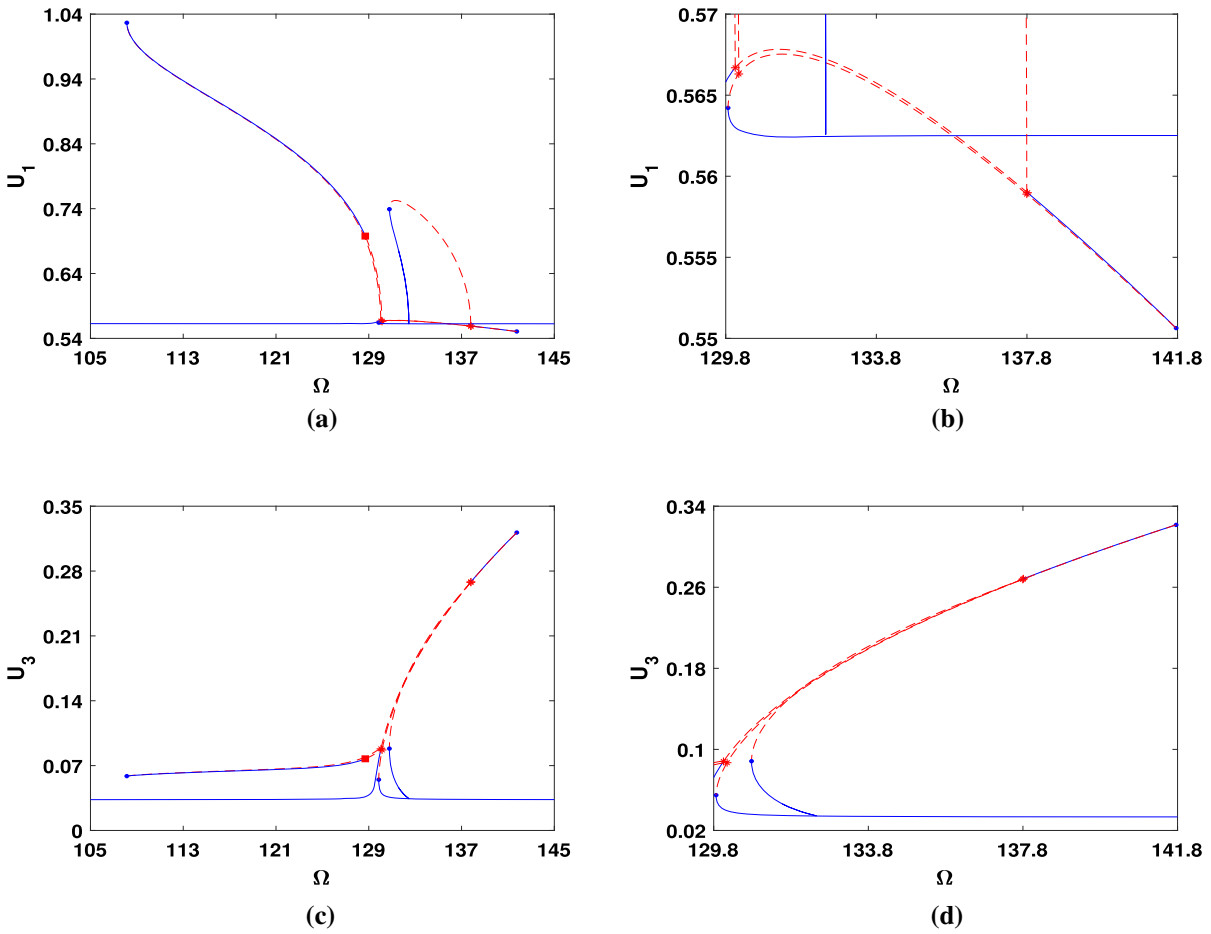

Fig. 25 Frequency response of the system at $V_{DC} = 195\ V$ and $V_{AC} = 0.2\ V$ for **a** first vibration mode , **b** closed view of the branching area of Fig. 25a, c Third vibration mode and d its correspondent closed view of the branching region in Fig. 25c

Neimark-Sacker points. The plots highlight that for applied sweeping frequency higher than $\Omega = 129.5$, the system tends to have limit point cycles at low applied AC voltage and lower period-doubling (torus) bifurcation thresholds.

To close this section, Fig. 27 displays the frequency response for $V_{DC} = 200\ V$ and $V_{AC} = 0.2\ V$. Compared to Fig. 20, we see that the system produces a higher response in the case of parametric

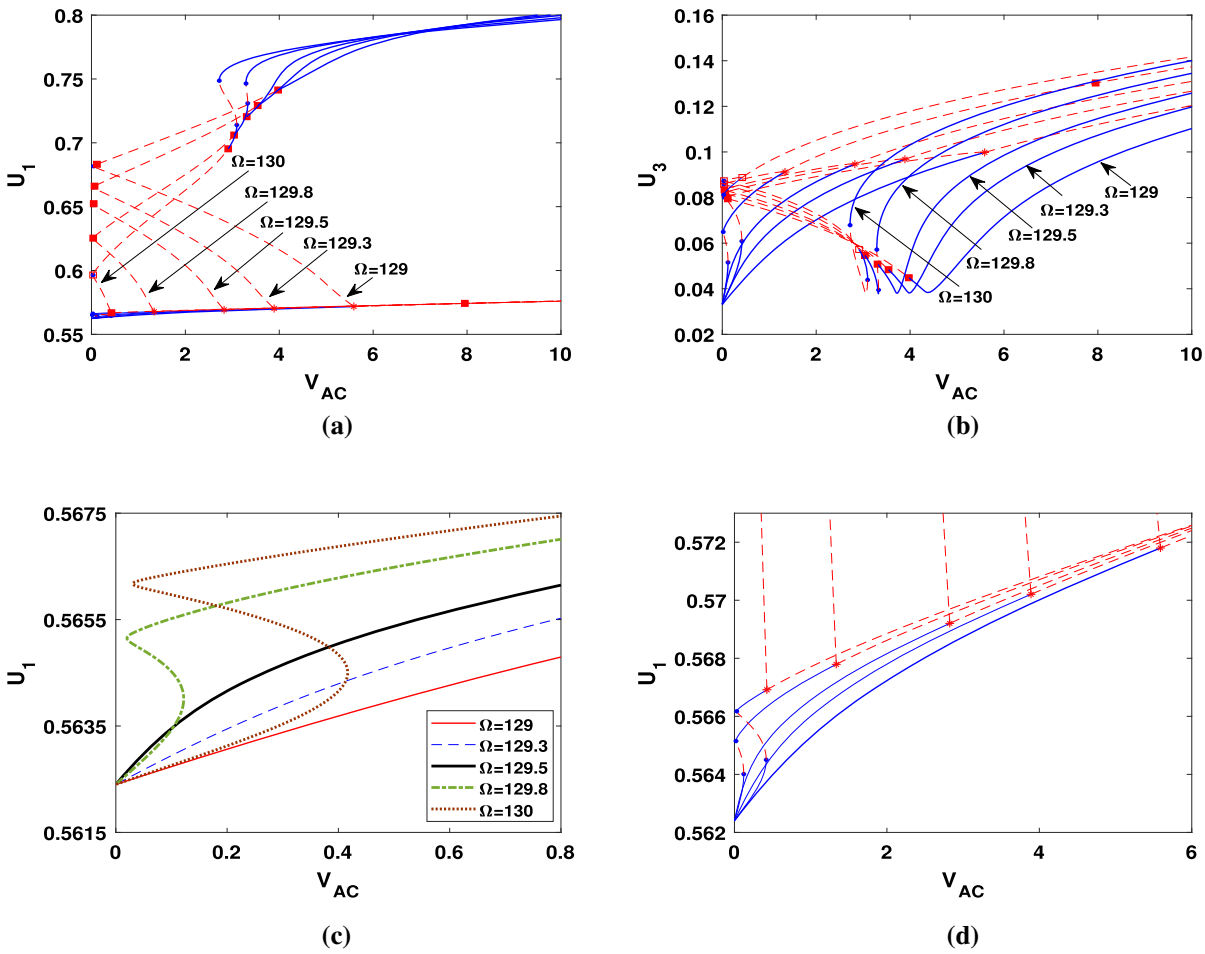

Fig. 26 Variation of force response at $V_{\mathrm{DC}} = 195$ for the **a** first and **c** third vibration mode, close-up of the branching area of Fig. 25a for **b** U_1 and **d** U_3

resonance. Along with the main response, the system exhibits an additional rising with half the magnitude of the main response. Again, this result can be applied to improve the system's performance for sensing/actuating applications. Moreover, the corresponding sub-figures depict the complicated nature of the system and branching regions with different bifurcation locus.

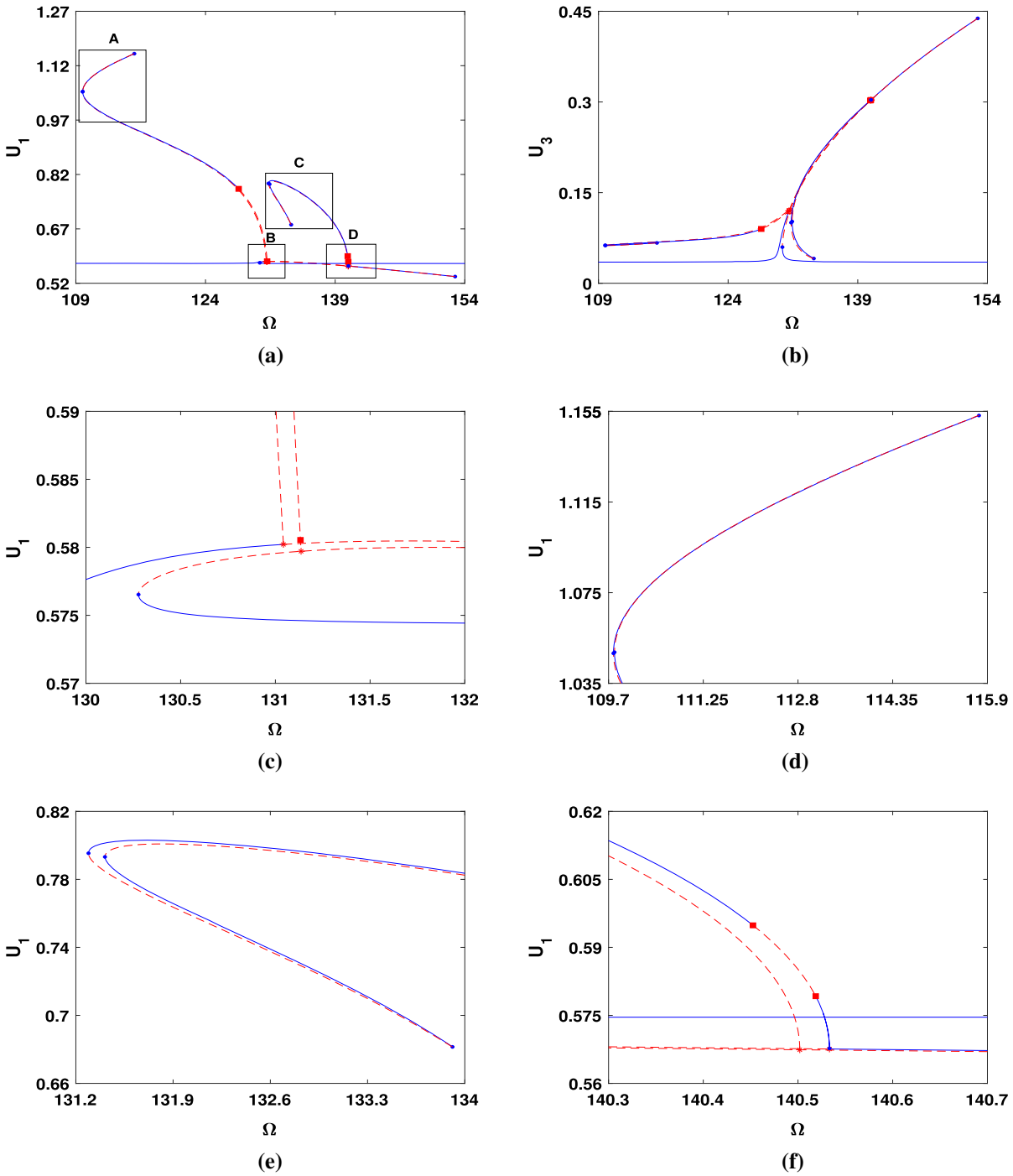

Fig. 27 Frequency response of the system at $V_{DC} = 200$ and $V_{AC} = 0.2\,V$ for **a** first vibration mode, **b** third vibration mode, and close-ups of **c** area A, **d** area B, **e** area C and **f** area D

4 Conclusion

In this paper, we have studied possibilities for the emergence of internal resonances in levitation force MEMS actuator in the case of CL and CC moving beams. First, we obtained the natural frequencies of modes up to third-order obtained by constructing the Jacobian matrix and then determined the ratio of these frequencies while varying the applied DC voltage.

In the case of the CL microbeam, the analysis shows that the prospect of internal resonance is low as the ratio of the frequencies is high. Lowering this ratio by increasing the length of the moving element led to a 5:1 internal resonance of the first and second modes. For higher values of the applied DC voltage, increasing the applied AC voltage can then magnify the results. The other important finding is related to the evaluation of the dominant factors of the system, including the applied AC and DC voltages that affect the thresholds for internal resonances to occur. Using simulations and bifurcation analysis, we efficiently computed the response curves, including turning points. We find a resonance tongue with bistability, while a single periodic response exists outside this region. The values for the applied DC voltage are in agreement with the linear analysis.

In the case of the CC microbeam as the moving element, our study revealed two regions: one in the vicinity of the primary resonance and one around the principal parametric resonance. Near the primary resonance, our study shows that increasing the applied DC voltage can intensify the energy exchange up to $V_{\mathrm{DC}} = 195\,V$ in which the applied AC voltage compensates for the reverse effect of the applied DC voltage. Beyond that value, the system loses the primary stroke response and shrinks to the second one, which increases for increasing applied AC voltage but never retrieves the main position. The force response deciphers the hidden features of the system by highlighting the bifurcation points in the vicinity of two applied frequency responses. The results show that in the applied frequency responses near activated internal resonance, the system displays multiple stable solution branches that is particularly effective for a resonant sensor.

For the principal parametric resonance, the system consisted of CC moving microbeam, exhibited more complex and rich dynamical behaviors showing strong possibilities of internal modes interactions. The generated frequency and force responses suggested an interesting system's capability to produce higher dynamic stroke as compared to its primary resonance. This outcome provides a platform for designing and modulating a micro-actuator with higher displacements and optimized dynamic performance. Furthermore, the analysis identified the period-doubling bifurcations. We have explored a MEMS layout with the capability of realizing a high travelling range through a repulsive force. As energy exchange among vibrational modes can enhance the frequency stabilization of self-sustained micro-resonators and compensate energy losses, this study can be instrumental for designing robust and efficient MEMS sensors and actuators, allowing to tune the system performances to accomplish the highest possible capabilities.

Moreover, by comparing the natural frequencies with and without the Von Karman nonlinearity for the CC microbeam, we found that the stretching term, by making the vibration modes approached to each other, is the origin of the internal resonances in our study rather than the repulsive force, which is then responsible for altering the response of the pre-interacted vibration modes.

Funding The authors have not disclosed any funding.

Data availability All data generated or analyzed during this study are included in this published article (and its supplementary information files).

Declarations

Conflict of interest The authors declare that they have no conflict of interest

References

1. Jafarsadeghi-pournaki, I., Rezazadeh, G., Zamanzadeh, M., Shabani, R.: Thermally induced vibration of an electrostatically deflected functionally graded micro-beam considering thermo-elastic coupling effect, Scientia Iranica 21 (3) (2014) 647–662. http://scientiairanica.sharif.edu/article_3503.html
2. Madinei, H., Zamanzadeh, M., Jafarsadeghi-pournaki, I., Rezazadeh, G.: Static pull-in analysis of capacitive FGM nanocantilevers subjected to thermal moment using Eringen's nonlocal elasticity. Int. J. Eng. **27**(4), 633–642 (2014). https://doi.org/10.5829/idosi.ije.2014.27.04a.15
3. Jafarsadeghi-Pournaki, I., Rezazadeh, G., Zamanzadeh, M., Shabani, R.: Parametric thermally induced vibration of an electrostatically deflected FGM micro-beam. Int. J. Appl. Mech. **8**(08), 1650092 (2016). https://doi.org/10.1142/S1758825116500927

4. Jafarsadeghi-Pournaki, I., Azizi, S., Zamanzadeh, M., Madinei, H., Shabani, R., Rezazadeh, G.: Size-dependent dynamics of a FG nanobeam near nonlinear resonances induced by heat. Appl. Math. Modell. **86**, 349–367 (2020). https://doi.org/10.1016/j.apm.2020.05.011
5. Pallay, M., Daeichin, M., Towfighian, S.: Dynamic behavior of an electrostatic MEMS resonator with repulsive actuation. Nonlinear Dyn. **89**(2), 1525–1538 (2017). https://doi.org/10.1007/s11071-017-3532-z
6. Pallay, M., Towfighian, S.: A parametric electrostatic resonator using repulsive force. Sens. Actuators A: Phys. **277**, 134–141 (2018). https://doi.org/10.1016/j.sna.2018.04.001
7. Zamanzadeh, M., Azizi, S.: Static and dynamic characterization of micro-electro-mechanical system repulsive force actuators. J. Vib. Control **26**(13–14), 1216–1231 (2020). https://doi.org/10.1177/1077546319892131
8. Pallay, M., Miles, R., Towfighian, S.: Merging parallel-plate and levitation actuators to enable linearity and tunability in electrostatic MEMS. J. Appl. Phys. **126**(1), 014501 (2019). https://doi.org/10.1063/1.5092980
9. Zamanzadeh, M., Jafarsadeghi-Pournaki, I., Ouakad, H.: A resonant pressure MEMS sensor based on levitation force excitation detection. Nonlinear Dyn. **100**, 1105–1123 (2020). https://doi.org/10.1007/s11071-020-05579-6
10. Pallay, M., Miles, R., Towfighian, S.: Towards a high bias voltage MEMS filter using electrostatic levitation. Mech. Syst. Signal Process. **150**, 107250 (2021). https://doi.org/10.1016/j.ymssp.2020.107250
11. Pallay, M., Miles, R., Towfighian, S.: A tunable electrostatic MEMS pressure switch. IEEE Trans. Ind. Electron. **67**(11), 9833–9840 (2019). https://doi.org/10.1109/TIE.2019.2956377
12. Pallay, M., Daeichin, M., Towfighian, S.: Feasibility study of a MEMS threshold-pressure sensor based on parametric resonance: experimental and theoretical investigations. J. Micromech. Microeng. **31**, 025002 (2021). https://doi.org/10.1088/1361-6439/abce9c
13. Zamanzadeh, M., Jafarsadeghi Pournaki, I., Azizi, S.: Bifurcation analysis of the levitation force MEMS actuators. Int. J. Mech. Sci. **178**, 105614 (2020). https://doi.org/10.1016/j.ijmecsci.2020.105614
14. Westra, H., Karabacak, D., Brongersma, S., Crego-Calama, M., Van Der Zant, H., Venstra, W.: Interactions between directly-and parametrically-driven vibration modes in a micromechanical resonator. Phys. Rev. B **84**(13), 134305 (2011). https://doi.org/10.1103/PhysRevB.84.134305
15. Asadi, K., Yu, J., Cho, H.: Nonlinear couplings and energy transfers in micro-and nano-mechanical resonators: intermodal coupling, internal resonance and synchronization. Phil. Trans. R. Soc. A. **376**(2127), 20170141 (2018). https://doi.org/10.1098/rsta.2017.0141
16. Younis, M., Nayfeh, A.: A study of the nonlinear response of a resonant microbeam to an electric actuation. Nonlinear Dyn. **31**(1), 91–117 (2003). https://doi.org/10.1023/A:1022103118330
17. Antonio, D., Zanette, D., López, D.: Frequency stabilization in nonlinear micromechanical oscillators. Nat. Commun. **3**(1), 806 (2012). https://doi.org/10.1038/ncomms1813
18. Ghayesh, M., Farokhi, H.: Size-dependent internal resonances and modal interactions in nonlinear dynamics of microcantilevers. Int. J. Mech. Mater. Des. **14**(1), 127–140 (2018). https://doi.org/10.1007/s10999-017-9365-6
19. Zhang, T., Guo, C., Jiang, Z., Wei, X.: Internal resonance between the extensional and flexural modes in micromechanical resonators. J. Appl. Phys. **126**(16), 164506 (2019). https://doi.org/10.1063/1.5115028
20. Kumar, P., Inamdar, M., Pawaskar, D.: Characterisation of the internal resonances of a clamped-clamped beam MEMS resonator. Microsyst. Technol. **26**, 1987–2003 (2020). https://doi.org/10.1007/s00542-020-04750-8
21. Ruzziconi, L., Jaber, N., Kosuru, L., Bellaredj, M., Younis, M.: Experimental and theoretical investigation of the 2: 1 internal resonance in the higher-order modes of a MEMS microbeam at elevated excitations. J. Sound Vib. **499**, 115983 (2021). https://doi.org/10.1016/j.jsv.2021.115983
22. Hajjaj, A., Hafiz, M., Younis, M.: Mode coupling and nonlinear resonances of MEMS arch resonators for bandpass filters. Sci. Rep. **7**, 41820 (2017). https://doi.org/10.1038/srep41820
23. Hajjaj, A., Alfosail, F., Younis, M.: Two-to-one internal resonance of MEMS arch resonators. Int. J. Non-Linear Mech. **107**, 64–72 (2018). https://doi.org/10.1016/j.ijnonlinmec.2018.09.014
24. Ouakad, H., Sedighi, H., Younis, M.: One-to-one and three-to-one internal resonances in MEMS shallow arches. J. Comput. Nonlinear Dyn. **12**(5), 051025 (2017). https://doi.org/10.1115/1.4036815
25. Wang, Z., Ren, J.: Three-to-one internal resonance in MEMS arch resonators. Sensors **19**(8), 1888 (2019). https://doi.org/10.3390/s19081888
26. Mangussi, F., Zanette, D.H.: Internal resonance in a vibrating beam: a zoo of nonlinear resonance peaks. PloS one **11**(9), e0162365 (2016). https://doi.org/10.1371/journal.pone.0162365
27. Younis, M., Abdel-Rahman, E., Nayfeh, A.: A reduced-order model for electrically actuated microbeam-based mems. J. Microelectromechanical Syst. **12**(5), 672–680 (2003). https://doi.org/10.1109/JMEMS.2003.818069
28. Zamanzadeh, M., Rezazadeh, G., Jafarsadeghi-Poornaki, I., Shabani, R.: Static and dynamic stability modeling of a capacitive FGM micro-beam in presence of temperature changes. Appl. Math. Modell. **37**(10–11), 6964–6978 (2013). https://doi.org/10.1016/j.apm.2013.02.034
29. Ouakad, H.M.: Electrostatic fringing-fields effects on the structural behavior of mems shallow arches. Microsyst. Technol. **24**(3), 1391–1399 (2018). https://doi.org/10.1007/s00542-016-2985-1
30. Zamanzadeh, M., Ouakad, H., Azizi, S.: Theoretical and experimental investigations of the primary and parametric resonances in repulsive force based MEMS actuators. Sens. Actuators A Phys. **303**, 111635 (2020). https://doi.org/10.1016/j.sna.2019.111635
31. Dhooge, A., Govaerts, W., Kuznetsov, Y.A., Meijer, H.G.E., Sautois, B.: New features of the software MatCont for bifurcation analysis of dynamical systems. Math. Comput. Modell. Dyn. Syst. **14**(2), 147–175 (2008). https://doi.org/10.1080/13873950701742754
32. Kuznetsov, Y.: Elements of Applied Bifurcation Theory, 3rd edn. Springer, Newyork (2004)

33. Younis, M.: MEMS linear and nonlinear statics and dynamics, of Microsystems, Springer Science & Business Media, 2011. https://doi.org/10.1007/978-1-4419-6020-7
34. Strogatz, S.H.: Nonlinear dynamics and chaos: with applications to physics, biology, chemistry, and engineering. CRC Press, United States (2018)
35. Sahoo, B., Panda, L., Pohit, G.: Two-frequency parametric excitation and internal resonance of a moving viscoelastic beam. Nonlinear Dyn. **82**(4), 1721–1742 (2015). https://doi.org/10.1007/s11071-015-2272-1
36. Sahoo, B., Panda, L., Pohit, G.: Combination, principal parametric and internal resonances of an accelerating beam under two frequency parametric excitation. Int. J. Non-Linear Mech. **78**, 35–44 (2016). https://doi.org/10.1016/j.ijnonlinmec.2015.09.017
37. Chin, C.-M., Nayfeh, A.: Three-to-one internal resonances in parametrically excited hinged-clamped beams. Nonlinear Dyn. **20**(2), 131–158 (1999). https://doi.org/10.1023/A:1008310419911
38. Ozdogan, M., Daeichin, M., Ramini, A., Towfighian, S.: Parametric resonance of a repulsive force MEMS electrostatic mirror. Sens. Actuators A Phys. **265**, 20–31 (2017). https://doi.org/10.1016/j.sna.2017.07.043